

A Study of Sea Ice Topography in the Weddell and Ross Seas Using Dual Polarimetric TanDEM-X Imagery

Lanqing Huang¹ and Irena Hajnsek^{1,2}

¹Institute of Environmental Engineering, Swiss Federal Institute of Technology in Zürich (ETH), Zürich, 8093, Switzerland

²Microwaves and Radar Institute, German Aerospace Center (DLR), Wessling, 82234, Germany

Correspondence: Lanqing Huang (huang@ifu.baug.ethz.ch)

Abstract. The sea ice topography is essential for understanding the interactions within the air-ocean-ice system

The total freeboard (snow+ice) is crucial for reflecting sea ice dynamics and interpreting the geophysical environments of polar oceans. Single-pass interferometric synthetic aperture radar (InSAR) allows for the generation of digital elevation mode~~DEM~~ models (DEMs) over the drift~~drifting~~ sea ice. However, accurate sea ice DEMs (i.e., snow~~total~~ freeboard) derived from

5 InSAR are impeded due to the radar signals penetrating the snow and ice layers. This research introduces a novel methodology for retrieving sea ice DEMs using dual-polarization interferometric SAR images, considering the variation in radar penetration bias across multiple ice types. The accuracy of the method is verified through photogrammetric measurements, demonstrating the derived DEM with a root-mean-square error of 0.26 m over a 200 × 19 km area. The method is further applied to broader regions in the Weddell and the Ross Sea, offering new insights into the regional variations of sea ice topography in
10 the Antarctic. We also characterize the non-Gaussian statistical behavior of sea ice elevations~~total freeboard~~ using log-normal and exponential-normal distributions. The results suggest that the exponential-normal distribution is superior in the thicker sea ice region (average elevation~~total freeboard~~ > 0.5 m), whereas the two distributions exhibit similar performance in the thinner ice region (average elevation~~total freeboard~~ < 0.5 m). These findings offer an in-depth representation of sea ice elevation~~total freeboard~~ and roughness in the Weddell and Ross Seas, which can be conducted in time series data to comprehend sea ice
15 dynamics, including its growth and deformation.

1 Introduction

The Sea ice topography refers to the ice shape, height, and large-scale roughness at the meter scale. It encompasses a variety of ice features, including rafted ice, ridges, rubble fields, and hummocks, all of which contribute to the intricate nature of sea ice topography (Weeks and Ackley, 1986). The presence of snow cover atop the ice surface further influences the topographic
20 characteristics, adding another layer of complexity to the overall sea ice topography (Massom et al., 2001).

The sea ice topography plays a crucial role in reflecting sea ice dynamics and interactions within the air-ocean-ice system. It showcases the spatial distribution of distinct surface features such as snow dunes (Trujillo et al., 2016; Iacozza and Barber, 1999) and deformed ice (Haas et al., 1999; Petty et al., 2016), which are impacted by the forces from winds and currents. Moreover,

the atmospheric drag coefficient over sea ice, which is topography-dependent, is an important parameter for understanding interactions at the ice-atmosphere boundary (Garbrecht et al., 2002; Castellani et al., 2014).

Sea ice topography can be described through digital elevation models (DEM). The DEM stands as an essential input into sea ice dynamic modeling, important for determining the air-ice drag coefficient and momentum flux (Garbrecht et al., 2002; Castellani et al., 2014). Moreover, the ~~snow freeboard~~ refers to the total freeboard (snow+ice) above the local sea surface. The DEM (i.e., snow freeboard) together with total freeboard can be converted to thickness with the knowledge of snow depth and the assumed values of snow, ice, and seawater densities, enables the determination of (Kwok and Kacimi, 2018). Estimating sea ice thickness (Kwok and Kacimi, 2018) offers valuable insights into the overall stability of sea ice in the changing climate. Furthermore, mapping sea ice topography is paramount for safe navigation in polar oceans. By providing information on ice deformation and identifying safe routes, accurate sea ice topography maps contribute to ensuring the safety and efficiency of ship navigation in challenging environments (Dammann et al., 2017).

Sea ice elevation has been measured DEMs can be obtained using laser altimeter mounted on different platforms, including helicopters (Dierking, 1995), aircraft such as IceBridge (Petty et al., 2016), and satellites like ICESat-1 (Zwally et al., 2008) and ICESat-2 (Kacimi and Kwok, 2020). These laser altimeters provide high-spatial resolution (< 1 m) in measuring sea ice elevation total freeboard. However, limited spatial coverage and long revisit times (e.g., 91 days for ICESat-2) restrict their capacity for consistent and comprehensive sea ice monitoring. In recent decades, synthetic aperture radar (SAR) has been of significant importance for Earth observation, offering a balance between spatial resolution (meters to tens of meters) and swath coverage (tens to hundreds of kilometers). SAR is unaffected by weather conditions or daylight limitations, enabling consistent data acquisition with a revisit time of around ten days. Notably, the advent of single-pass interferometric SAR (InSAR) sensors, exemplified by TanDEM-X, presents an unprecedented opportunity to generate sea ice DEMs for drift (Dierking et al., 2017) and landfast (Yitayew et al., 2018) sea ice over landfast sea ice (Dierking et al., 2017; Yitayew et al., 2018). For drifting ice, the accuracy of InSAR-derived DEMs can be affected by additional phase shifts induced by ice motion. Dierking et al. (2017) calculated and theoretically discussed the sensitivity of InSAR-derived DEMs concerning ice-drifting velocity, InSAR frequency, and baseline configuration.

Nevertheless, the InSAR-derived DEM can be affected by the microwave penetration into the snow and ice layers. Dry snow can have penetration depths up to hundreds of wavelengths (Guneriusson et al., 2001). For X-band SAR, the penetration into younger ice, such as new and first-year ice, is minimal due to the high salinity of the ice surface (Hallikainen and Winebrenner, 1992). On the other hand, for older and desalinated ice, such as multi-year ice, the penetration depth varies from 0 – 1 m depending on the temperature and salinity (Hallikainen and Winebrenner, 1992; Huang et al., 2021). To account for the scattering mechanism from the volumes (snow and ice) and layers (snow-ice-water interfaces), a two-layer-plus-volume (TLPV) model (Huang et al., 2021) has been developed to determine the penetration depth over snow-covered old ice in the Antarctic. The model improves the precision of sea ice topographic mapping by offsetting the InSAR phase center to the top surface.

SAR polarimetry complements interferometry by providing valuable insights into scattering processes and has proven useful for characterizing sea ice properties (Winebrenner et al., 1995; Ressel et al., 2016; Singha et al., 2018). For old and deformed

ice, a radar theory has been developed to examine the relationship between scattering mechanisms and sea ice DEM (Nghiem et al., 2022), resulting in a geophysical model function based on co-polarimetric coherence for retrieving sea ice DEM (Huang et al., 2022). These findings emphasize the significance of integrating polarimetric and interferometric information for ~~precise accurate~~ sea ice topography mapping using SAR imagery.

Given the variations in the microwaves' penetration depth into snow and ice, deriving sea ice DEM from SAR imagery over a broad spatial scale encompassing diverse ice types is still constrained. In this study, we develop an innovative two-step method to generate sea ice DEM across multiple ice types using machine learning and polarimetric-interferometry SAR techniques. The initial step involves the development of a random forest classifier using specific SAR features to categorize sea ice into two groups: ~~younger ice (YI) and older ice (OI)~~ ~~small-penetration condition ice (SPI) and large-penetration condition ice (LPI)~~, based on the penetration depth of microwaves ~~into the snow and ice~~. Subsequently, a sea ice DEM is created for each ice type. In the case of ~~YI~~ ~~SPI~~, standard InSAR processing is applied to determine the ~~elevation~~. For ~~OI~~ ~~total freeboard~~, For ~~LPI~~, a novel 70 inversion algorithm is proposed to estimate the parameters of the developed TLPV model (Huang et al., 2021). This ~~model~~ allows for correcting penetration bias in the InSAR signal over ~~OILPI~~, resulting in ~~a precise sea ice DEM~~ ~~an accurate retrieval of the total freeboard~~. We validate the proposed method against the photogrammetric DEM from the IceBridge aircraft. A root-mean-square error (RMSE) of 0.26 m between the derived DEM and reference data ~~signifies a precise elevation mapping for both YI and OI. Throughout the paper, "sea ice elevation" is the entire vertical height (including snow depth) above the local sea surface. indicates an improved accuracy in total freeboard retrieval~~.

We further implement the proposed two-step approach to 162 SAR images covering 12 segments (each covering an area of $\sim 500 \times 20$ km) in the Weddell and Ross ~~Sea Seas~~. This allows a broad mapping of sea ice ~~elevation DEM~~ and roughness, offering new insights into the topographic patterns of sea ice at a large spatial scale. Note that the roughness in this study refers to the macroscale roughness, which is defined as the standard deviation of ~~elevation total freeboard~~ within 50×50 m window. We analyze the variation in sea ice ~~elevation DEM~~ and roughness along the southwards direction and associate it with the variation in sea ice classes obtained from ~~the Ice Chart~~ ~~an operational product from the U.S. National Ice Center~~. The statistics of ~~sea ice elevations total freeboard~~ over various regions are modeled using the log-normal and exponential-modified normal distributions. The findings enhance our understanding of sea ice formation and dynamics and can be used to interpret geophysical parameters associated with sea ice topography.

85 The paper is structured as follows. Section 2 describes the data sets and data processing procedures. The two-step approach for sea ice DEM retrieval is introduced in Sect. 3. The retrieval results and interpretation of topographic characteristics are ~~discussed given~~ in Sect. 4 ~~and further discussed in Sect. 5~~. Finally, Section 6 ~~concludes summarizes~~ the study.

2 Data sets and processing

2.1 Study area

90 The region of interest includes both the Weddell Sea and the Ross Sea, as shown in Fig. 1. The SAR footprints over the two seas are zoomed-in in boxes A and B, respectively. The footprints ~~comprise~~ ~~consist of~~ 12 segments, each corresponding to a

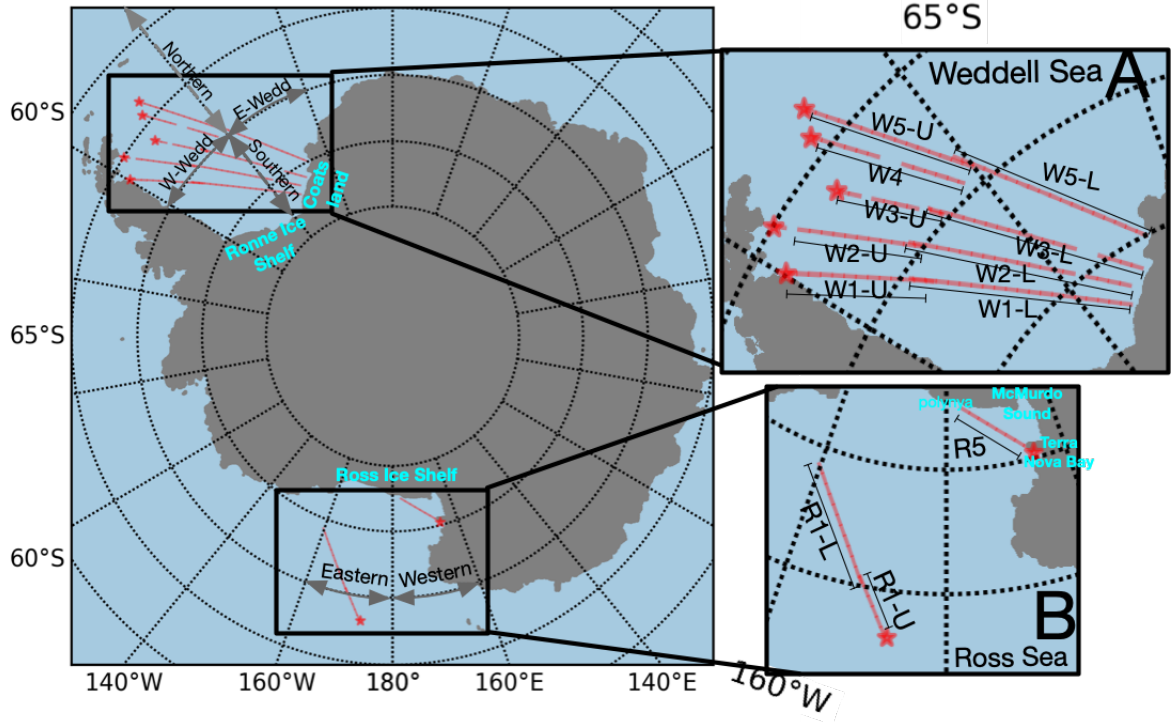


Figure 1. Geolocation of the study area. The northernmost positions in each segment are marked with star symbols and serve as reference points for calculating the relative distance in Sec. 4.2.

sequence of SAR ~~acquisitions at almost images within the same orbit, all acquired at nearly~~ the same timestamp, with only seconds varying between them. The segments will be referred to as W1-U, W1-L, W2-U, W2-L, W3-U, W3-L, W4, W5-U, W5-L, R1-U, R1-L, and R5 in the following sections for conciseness.

95 2.2 SAR Imagery

The TanDEM-X is a SAR interferometer that operates as a bistatic single-pass system, capable of acquiring two images simultaneously (Krieger et al., 2007). The two images are co-registered single-look complex products, which can be processed to derive sea ice DEM through interferometry.

In the study, we collected 162 SAR images over the twelve segments in StripMap mode in dual-pol channels (HH and VV).
100 The pixel spacing is around $0.9\text{ m} \times 2.7\text{ m}$ in slant range and azimuth. The acquisition time and the number of images for each segment are listed in Table 1. The incidence angle (InA) is measured at the center of the scene, and the height of ambiguity (HoA) corresponds to an interferometric phase change of 2π . Note that for R5, the larger HoA leads to a relatively higher

Table 1. Summary of SAR acquisitions and Ice Charts over the study area.

Segment	Number of SAR images	SAR acquisition time	HoA(m)	InA($^{\circ}$)	Weekly average Ice Charts (ending date)
W1-L	20	2017-10-24T23:30	30 – 35	29	2017-10-26
W1-U	13	2017-10-29T23:41	33 – 35	35	2017-11-02
W2-L	19	2017-10-25T23:13	30 – 35	29	2017-10-26
W2-U	12	2017-10-30T23:23	32 – 34	35	2017-11-02
W3-L	18	2017-10-26T22:56	30 – 35	29	2017-11-02
W3-U	8	2017-11-22T23:05	36 – 37	35	2017-11-23
W4	12	2017-11-01T22:49	32 – 34	35	2017-11-02
W5-L	18	2017-11-02T22:30	30 – 34	29	2017-11-09
W5-U	15	2017-10-27T22:41	31 – 34	35	2017-11-02
R1-L	12	2017-11-11T07:16	33 – 35	31	2017-11-16
R1-U	6	2017-10-25T07:25	34 – 35	36	2017-10-26
R5	9	2017-11-07T09:58	40 – 42	35	2017-11-09

average uncertainty in the derived InSAR height (h_{InSAR}) compared to other InSAR configurations with smaller HoA. More details can be found in the appendix A1.

105 The multilooking processing was conducted using a 4×12 window, resulting in a $\sim 10 \times 10$ m pixel spacing in azimuth and range – ground range. This resolution ($\sim 10 \times 10$ m) was subsequently utilized for the sea ice classification and DEM retrieval detailed in Section 3. The backscattering intensity σ_{measure} of the images includes additive thermal noise, which can be described by the noise equivalent sigma zero (NESZ) and assumed to be uncorrelated with the signal (Nghiem et al., 1995). Removing the thermal noise allows for a better representation of sea ice features, which is crucial for ice classification. We 110 denoised backscattering intensities for the different polarizations (i.e., HH, VV, Pauli-1 (HH+VV), and Pauli-2 (HH-VV)) by subtracting the noise equivalent sigma zero (NESZ) from the σ_{measure} (Huang et al., 2022). These denoised More details about the thermal noise removal can be found in the appendix A2. The denoised backscattering intensities are used in the following sections.

2.3 Optical Digital Mapping System (DMS) data

115 With an objective to investigate Antarctic sea ice topography, Operation IceBridge (OIB) and TanDEM-X Antarctic Science Campaign (OTASC) (Nghiem et al., 2018) was successfully carried out along a portion of the W1, shown in Fig. 2a. Equipped with a digital mapping system (DMS), the OIB aircraft captured optical images (Dominguez, 2010, updated 2018) and generated DEM using photogrammetric techniques at a spatial resolution of approximately 40 cm \times 40 cm with a vertical accuracy of 0.2 m (Dotson and Arvesen., 2012, updated 2014). The DMS acquisitions occurred between 17:45 and 18:44 UTC on October

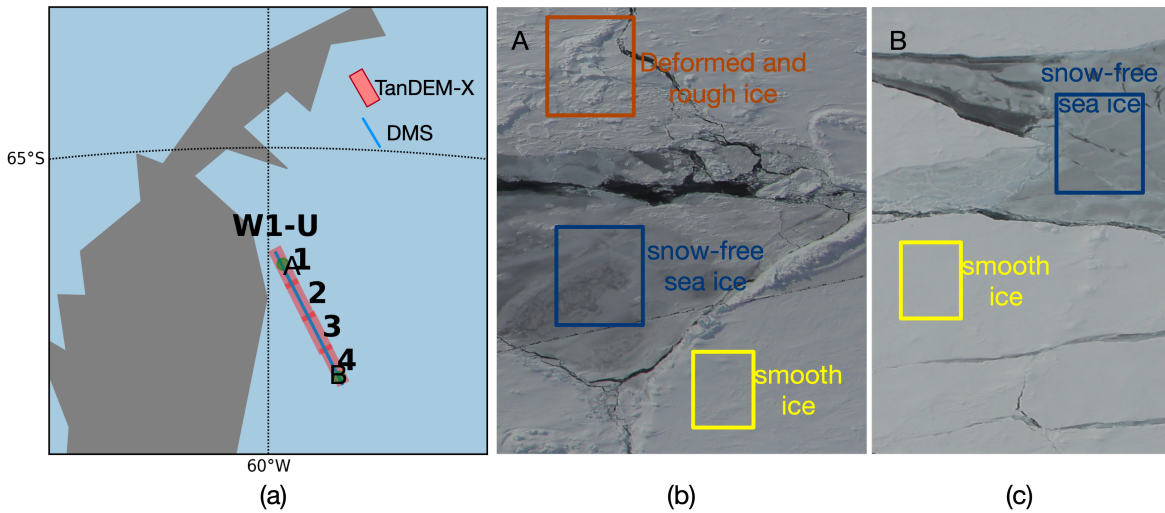


Figure 2. (a) Geolocation of DMS measurements superimposed on four SAR footprints in segment W1-U. Zoomed-in views of DMS digital images at points A and B (green dots) are displayed in (b) and (c), respectively.

120 29, 2017. Figure 2b and c showcase DMS optical images over specific areas, highlighting a diverse range of sea ice features, including ridges, deformed ice, smooth ice with snow cover, and snow-free ice.

In this study, we geocoded the DMS DEM to match the same coordinates and resolution as the multilooked SAR image, which is approximately 10×10 m in both range and azimuth. The calibration of the Note that DMS DEM gives height values relative to the WGS-84 ellipsoid. To obtain the total freeboard, we calibrated the DMS DEM to the local sea level was 125 accomplished through a manual process involving the selection of the water surface from DMS images (Huang et al., 2021). The calibrated DMS DEM, henceforth is referred to as DMS DEM for brevity.

As the sea ice is constantly moving, co-registration is crucial to compensate for the time lag (~ 6 hours) between the DMS sensor and TanDEM-X. To achieve this, we carefully aligned the two data by identifying distinctive sea ice features in both optical and SAR images (Huang et al., 2021, 2022). Note that the segments lacking distinctive sea ice features in optical and 130 SAR images were eliminated to ensure co-registration quality. The co-registered DMS DEM is used as reference data in this study.

2.4 Ice Charts

Weekly sea ice concentration The U.S. National Ice Center's Antarctic sea ice charts (referred to as Ice Charts hereafter) 135 represent the average offer weekly products detailing total sea ice concentration, partial concentration, and stage of development along with respective concentrations over a 7-day period (U.S. National Ice Center., 2022). (U.S. National Ice Center., 2022)

The Ice Charts covering the date of SAR acquisitions are listed in Table 1.

Table 2. Stage of develops for ice type categories (U.S. National Ice Center, 2022).

Ice Stage of development	Thickness (cm)	Ice type
New ice	< 10	
Nilas, ice rind	< 10	
Young ice	10 – < 30	Thin ice (TI)
Gray ice	10 – < 15	
Gray-white ice	15 – < 30	
FYI	≥ 30 – 200	
Thin FYI	30 – < 70	
Medium FYI	70 – < 120	First-year ice (FYI)
Thick FYI	≥ 120	
Old ice		
2nd year ice	N/A	Multiyear ice (MYI)
multiyear ice		

The Ice Charts are provided in Shapefile format as grids with a spatial resolution of 10×10 km. For each specified latitude and longitude, three ice concentration values are given, each corresponding to a different stage of ice development. Details of these stages and their corresponding thicknesses can be found in the first and second columns of Table 2, respectively.

140 The postprocessing of the Ice Charts consists of two steps. First, we categorized the three stages of ice into thin ice (TI), first-year ice (FYI), and multiyear ice (MYI) types according to the third column of Table 2. Next, we ~~calculated the average ice type by $\sum_{i=1}^3 IC_i \times IT_i$, where IC_i denotes the ice concentration value and IT_i stands for the ice type index for each stage i . Ice-type indices (IT_i) are assigned as 0 for TI, 1 for extracted the ice concentration values for TI, FYI, and 2 for MYI MYI, respectively.~~

2.5 SAR interferometry

145 Single-pass interferometer acquires two simultaneous observations, denoted as s_1 and s_2 . The complex interferogram γ and the interferometric phase ϕ_γ can be described as (Cloude, 2010)

$$\gamma = s_1 s_2^* \quad (1)$$

$$\phi_\gamma = \arg\{s_1 s_2^*\} \quad (2)$$

150 The further processing of ϕ_γ includes flat earth removal, interferogram filtering, low-coherence area mask, and phase unwrapping (Huang and Hajnsek, 2021). The resulting ϕ'_γ ~~is can be~~ converted to height by

$$h_{\text{InSAR}} = h_a \frac{\phi'_\gamma}{2\pi} \quad (3)$$

where h_{InSAR} is the height of InSAR phase center and h_a is the HoA related to the InSAR baseline configuration provided in Table 1.

155 The complex interferometric coherence $\tilde{\gamma}_{\text{InSAR}}$ between the two images can be estimated by (Cloude, 2010)

$$\tilde{\gamma}_{\text{InSAR}} = \gamma_{\text{InSAR}} \cdot e^{i\phi_{\gamma}} = \frac{< s_1 s_2^* >}{\sqrt{< s_1 s_1^* > < s_2 s_2^* >}} \quad (4)$$

where the symbol $< . >$ denotes an ensemble average within a 4×12 multilooking window. Pixels with $\gamma_{\text{InSAR}} < 0.3$ were designated as water areas and excluded from further processing. The above interferometric processing was carried out using the GAMMA software.

160 The h_{InSAR} obtained from Eq. 3 was further calibrated to the average water surface. Instead of identifying water pixels that were masked out due to the low InSAR coherence (less than 0.3), we selected smooth and new ice regions, assuming they are thin enough and their elevation (i.e., radar freeboard) is negligible and approximately equal to the water surface. The smooth and thin ice regions typically exhibit very low backscattering intensities in SAR image (Dierking et al., 2017). Therefore, we selected pixels with backscattering intensities within the range of -19 dB to -18 dB , slightly above TanDEM-X's noise level (-19 dB), and generated a histogram of h_{InSAR} values for these pixels. We determined the 3rd percentile of the height of these pixels as the water surface elevation. The threshold value, i.e., the 3rd percentile, was chosen based on applying the method to four SAR scenarios overlaid with DMS DEM. By choosing the 3rd percentile as the water surface level, we ensured alignment between the water surface levels derived from InSAR and those from the DMS data, thus validating the threshold value. Note that we estimate a single value representing the water surface for each SAR scene. However, it's important to note that this 165 method may introduce inaccuracies due to the centimeter-level radar freeboard of the selected thin and new ice, as well as the fluctuating water surface within each SAR scenario.

170

2.6 SAR polarimetry

SAR Polarimetry reflects scattering mechanisms and has been proven as a proxy for characterizing sea ice properties (Wakabayashi et al., 2004; Ressel et al., 2016; Huang and Hajnsek, 2021; Singha et al., 2018; Nghiem et al., 2022).

175 2.6.1 Co-polarization ratio

The co-polarization (coPol) ratio (R_{coPol}) measures the backscattering intensity ratio between the dual-pol channels and can be calculated as follows

$$R_{\text{coPol}} = \frac{\sigma_{\text{HH}}}{\sigma_{\text{VV}}} \quad (5)$$

where σ_{HH} and σ_{VV} are denoised SAR backscattering intensity in dual-pol channels in linear scale. R_{coPol} related to extracted from L-band SAR images is associated with the dielectric constant, has been considered and has therefore been used as an indicator for ice thickness (Wakabayashi et al., 2004). Further investigation is required to determine if R_{coPol} from the X-band can also serve as a proxy for ice thickness. Additionally, R_{coPol} has been identified as an important feature for

discriminating thicker ice and water and is an effective tool for classifying sea ice in X-band SAR imagery (Ressel et al., 2016).

185 2.6.2 Pauli-polarization ratio

Similarly, we can obtain the Pauli-polarization ratio (R_{pauli}) by

$$R_{\text{pauli}} = \frac{\sigma_{\text{P1}}}{\sigma_{\text{P2}}} = \frac{|s_{\text{HH}} + s_{\text{VV}}|^2}{|s_{\text{HH}} - s_{\text{VV}}|^2} \quad (6)$$

where σ_{P1} and σ_{P2} are denoised SAR backscattering intensity in Pauli-1 and Pauli-2 polarizations in linear scale, respectively. s_{HH} and s_{VV} are single-look complex images in dual-pol channels, respectively.

190 2.6.3 Complex coPol coherence

The complex coPol correlation $\tilde{\gamma}_{\text{coPol}}$ is calculated as (Lee and Pottier, 2009)

$$\tilde{\gamma}_{\text{coPol}} = \gamma_{\text{coPol}} \cdot e^{i\phi_{\text{coPol}}} = \frac{< s_{\text{VV}} s_{\text{HH}}^* >}{\sqrt{< s_{\text{VV}} s_{\text{VV}}^* > < s_{\text{HH}} s_{\text{HH}}^* >}} \quad (7)$$

where γ_{coPol} is the coPol coherence magnitude and ϕ_{coPol} is the coPol phase. s_{HH} and s_{VV} are single-look complex images in dual-pol channels, respectively.

195 γ_{coPol} measures the degree of electromagnetic wave depolarization caused by the surface roughness and the volume scattering. This parameter has been shown to be associated with sea ice ~~elevation DEM~~ (Huang and Hajnsek, 2021) and thickness (Kim et al., 2011). ϕ_{coPol} is sensitive to the anisotropic structure of the medium and deviates from 0° when the signal delay becomes polarization dependent (Leinss et al., 2014). ϕ_{coPol} has been utilized in retrieving fresh-snow anisotropy over ground (Leinss et al., 2016) and characterizing the topography of snow layer (Huang and Hajnsek, 2021).

200 3 Methodology

This section introduces an innovative ~~two-step~~ approach for retrieving sea ice ~~elevation DEM~~ across various ice conditions, shown in Fig. 3. The initial step is categorizing sea ice into ~~OI and YI~~ LPI and SPI types based on radar penetration depths. The second step involves generating the sea ice DEM using different methods for the two ~~sea~~ ice categories. The ~~two steps~~ ~~two-step approach is presented in Fig. 3(a) and~~ are detailed in Sect. 3.1 and Sect. 3.2, respectively. The method is developed 205 and validated using the four SAR images (Fig. 2) overlapped with DMS DEM, ~~see Fig. 2.~~

3.1 Sea ice classification

The ~~As shown in Fig. 3(a), in Step 1, the sea ice is classified into SPI and LPI using a~~ random forest (RF) classifier (Breiman, 2001) ~~is implemented to categorize sea ice, shown~~. A detailed description of the training and validating process for the classifier ~~is given in Fig. ??, where SAR images and~~ 3(b), where DMS DEM (h_{DMS}) are utilized as ~~inputs into the proposed flowchart~~

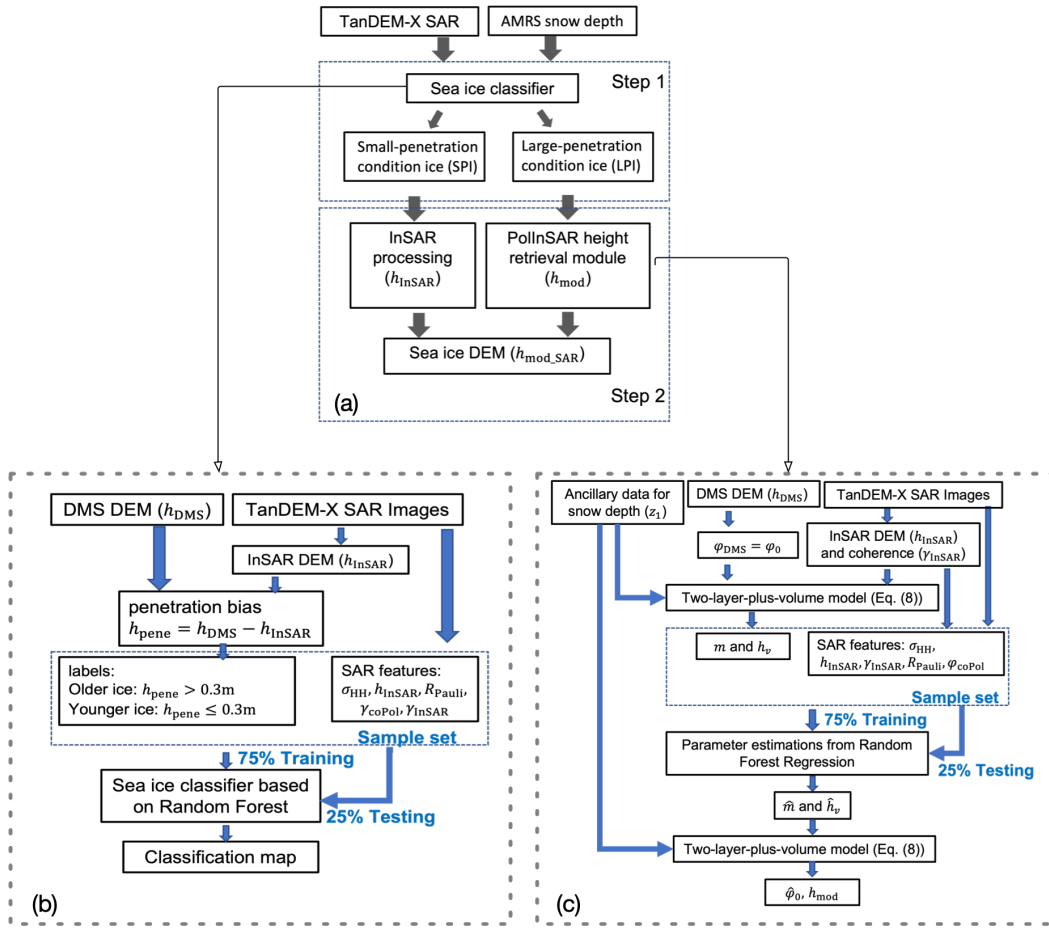


Figure 3. (a) The proposed two-step approach for sea ice DEM retrieval. (b) The details (training and validation) of the sea ice classifier and (c) the PolInSAR height retrieval module are illustrated in Fig. ?? and ??, respectively.

210 **reference data.** The penetration depth $h_{\text{pene}} = h_{\text{DMS}} - h_{\text{InSAR}}$, where h_{DMS} measures the total freeboard, i.e., elevation from the snow-air surface relative to the seawaterwater level. InSAR DEM (h_{InSAR}) measures the radar freeboard, i.e., the elevation of the InSAR phase center relative to the water level, which can be somewhere inside of the snow or ice, depending on the snow and ice condition. h_{InSAR} is generated from TanDEM-X InSAR pair following the principles in Sect. 2.5. In general, microwaves can penetrate much shallower into the younger and more saline compared to the older and less saline

215 sea ice (Hallikainen and Winebrenner, 1992). The sea ice penetration depth over multiyear ice is suggested to be 0.3 – 1 m at the X-band, which varies with temperature Hallikainen and Winebrenner (1992). Desalination within ice ridges increases the effective penetration depth compared to level ice (Dierking et al., 2017). Considering these findings and given the study area's snow cover and the presence of deformed ice formations such as ridges, we chose a penetration depth of 0.3 m as the threshold

for distinguishing the two ice types. Hence, pixels with $h_{\text{pene}} < 0.3 \text{ m}$ are labeled as **YI**SPI, whereas those with $h_{\text{pene}} \leq 0.3 \text{ m}$

220 are **OI** $h_{\text{pene}} \geq 0.3 \text{ m}$ are LPI.

Flowchart for sea ice classification.

We investigate a range of features for classification, including denoised backscattering intensity in HH polarization (σ_{HH}), polarimetric features such as coPol ratio (R_{coPol}), Pauli-polarization ratio (R_{Pauli}), coPol coherence magnitude (γ_{coPol}), and coPol phase (ϕ_{coPol}), as well as interferometric features including InSAR coherence magnitude (γ_{InSAR}) and height 225 of interferometric phase center (h_{InSAR}). To improve computational performance, we rank features based on Gini Importance (i.e., Mean Decrease in Impurity), which measures the average gain of purity by splits of a given variable. The ranking of the features is illustrated in Fig. A3, where the top five features, i.e., R_{Pauli} , σ_{HH} , h_{InSAR} , γ_{coPol} , and γ_{InSAR} are selected as effective predictors for the RF classifier. The ranking of all the SAR features is given in the appendix Fig. A3. Note that the 230 computed Gini importance is not inherently specific to a particular class or ice type. Instead, it represents the relative importance of features in making overall classification decisions within the context of the entire dataset. Therefore, the importance level determined by Gini importance is not specific to individual ice types but reflects the significance of features for the classifier's overall predictive performance across all classes.

The selected features together with the ice labels (i.e., **OI** and **YI** and **LPI** and **SPI**) form the sample set. 75% is used for training the RF classifier, implemented in Python using default hyperparameters. Since sample numbers for the **YI** and **OI** and **SPI** and 235 **LPI** classes are well-balanced (48% and 52%, respectively), no balanced training strategy is particularly implemented. The validation of ice classification over the testing subset (25%) will be given in Sect. 4.1.

Gini importance computed from the Random Forest (RF) classifier.

3.2 DEM generation

Based on the classification map, As shown in Fig. 3(a), in Step 2, we separately retrieve the sea ice elevations DEMs for the 240 two categories of ice . For YI based on the classification map. For SPI, the conventional InSAR processing (Section 2.5) is conducted, given the minimal penetration depth attributed to the saline ice. On the other hand, for OI LPI which is subject to radar signal penetration, we apply the TLPV model developed in (Huang et al., 2021), which incorporates InSAR processing and corrects for the radar penetration bias into the snow-covered old ice.

The TLPV model includes surface scattering from the top and bottom interfaces and volumes scattering from the snow and 245 ice, shown in Fig. 4. The model was further simplified by merging the contributions of the snow volume, the ice volume, and the top layer into one Dirac delta (Huang et al., 2021):

$$\begin{aligned} \tilde{\gamma}_{\text{InSAR}} &\approx e^{i\phi_0} \frac{1 \cdot e^{i\phi_1} + m \cdot e^{i\phi_2}}{1 + m} \\ &= e^{i\phi_0} \tilde{\gamma}_{\text{mod}}(m, z_1, z_2) \\ &= e^{i\phi_0} \tilde{\gamma}_{\text{mod}}(m, z_1, h_v) \end{aligned} \tag{8}$$

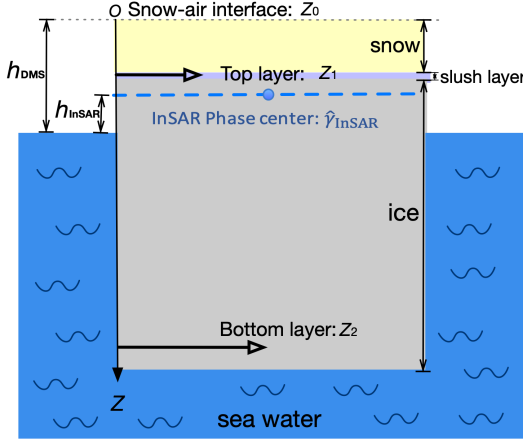


Figure 4. The schematic of the proposed TLPV model for sea ice (Huang et al., 2021).

where ϕ_0 is the topographic phase at the snow-air interface, m refers to the layer-to-layer ratio, $\phi_1 = \kappa_{z_vol}z_1$, $\phi_2 = \kappa_{z_vol}z_2$, z_1 and z_2 are the locations of the layers, respectively. $h_v = z_1 - z_2$ refers to the depth between the top and bottom layer. It's worth

250 noting that the bottom layer may not always be at the ice-water interface. In certain situations, there might be a lower basal saline ice layer, inducing strong surface scattering from the ice-basal layer interface (Nghiem et al., 2022). This basal saline layer contains brine inclusions with higher salinity, transitioning towards the ice-seawater interface (Tison et al., 2008). κ_{z_vol} is the vertical wavenumber in the volume which depends on the InSAR configuration such as HoA and the incidence angle, and the dielectric constant of the volume (Dall, 2007; Sharma et al., 2012; Huang et al., 2021). m refers to the layer-to-layer ratio, which is the backscattering power ratio between the top and bottom layer:

$$m = \frac{\sigma_{bottom}(\omega)}{\sigma_{top}(\omega)} \quad (9)$$

where $\sigma_{top}(\omega)$ and $\sigma_{bottom}(\omega)$ denotes the backscattering power from the top and bottom interface, respectively, at a given polarization ω . m potentially reveals the relative importance of scattering from these interfaces, depending on factors like interface roughness, dielectric constant, and radar polarization. A larger value of m signifies that surface scattering from the bottom layer predominates, while a smaller m indicates that surface scattering from the top layer is more significant.

260 The aim is to estimate ϕ_0 and convert it into height (h_{mod}), which is the total freeboard of LPI. When fixing the origin at the air-snow interface, z_1 is equivalent to snow depth, which can be obtained from the AMSR Level-3 data (Meier et al., 2018). However, Eq. (8) still contains two unknown variables, m and h_v , preventing direct estimation of ϕ_0 .

PolInSAR height retrieval module:

265 To address the above issue Therefore, we develop a new algorithm PolInSAR height retrieval module to invert the TLPV model and estimate m and h_v from SAR observations using RF regression, illustrated, shown in Fig. ???. The RF regressor is trained using the same sample set as the sea ice classification. 3(c). We first establish an empirical relation (RF regression) between SAR features and the true values of m and h_v which can be derived using DMS DEM as a priori information.

Specifically, we simulate the interferometric phase ($\phi_{\text{DMS}} = \phi_0$) from the height (h_{DMS} can be transformed into ϕ_{DMS} by) 270 using Eq. (3) and input as a priori information. With the above specific parameters, tailored to the specific InSAR configuration with h_a given in Table 1. With snow depth z_1 and γ_{InSAR} from AMSR data and InSAR observations, respectively, m and h_v values can be derived by inverting Eq. (8) and used as true values for training the RF regressor.

We also use Gini Importance to rank the seven features for regression, selecting the top five predictors for estimating m and h_v : σ_{HH} , h_{InSAR} , γ_{InSAR} , R_{Pauli} , and ϕ_{coPol} , shown in. The ranking of all the SAR features 275 is given in the appendix Fig. A4. The selected features, together with the derived true m and h_v , form the sample set that is partitioned into training (75%) and testing subsets (25%). is used for training the RF regressor. Note that the RF regressor is trained using the same sample set as the sea ice classification.

The selected features from InSAR observations The well-trained RF regressor is subsequently utilized to estimate \hat{m} and \hat{h}_v for SAR scenes that do not overlap with DMS measurements. Selected features from SAR images, along with z_1 from ancillary 280 data, are input into the well-trained serve as inputs to the RF regression model to estimate for estimating \hat{m} and \hat{h}_v over the testing set. Then. Subsequently, the topographic phase $\hat{\phi}_0$ can be derived by solving Eq. (8), and transformed into elevation transformed into total freeboard h_{mod} by using Eq. (3). The For SAR scenes overlaid with DMS measurements, validation of height retrieval accuracy over the testing subset (25%) will be given in the next section Sect. 4.1.

Gini importance computed from the Random Forest (RF) regressor for estimating m and h_v .

285 4 Results

Following the two-step approach developed in Sect. 3, this section obtains the SAR-derived DEM from 162 dual-pol InSAR pairs that cover the sea ice in the Weddell and Ross Seas. We verify the accuracy of the SAR-derived DEM. We further analyze the variation of elevation total freeboard and roughness along the southward direction and examine the statistical characteristics of sea ice elevation DEM across various geographic regions.

290 4.1 Sea ice topography retrieval and validation

The proposed two-step approach for sea ice elevation DEM retrieval is visually and quantitatively validated based on the four scenes overlapped with DMS measurements. The SAR backscattering intensities over the four scenes are displayed in the left column in Fig. 5. In the first step, the proposed classification scheme (Fig. ??) demonstrates good performance on the testing set, with an accuracy of 0.84 and a confusion matrix presented in Fig. 6(a). The classifier is then applied to the entire SAR 295 images, including the region not overlapped by DMS DEM, and the classified maps are shown in the middle column of Fig. 5.

In the second step, the sea ice DEM ($h_{\text{mod_SAR}}$) is obtained by merging h_{mod} and h_{InSAR} over OI and YI, LPI and SPI. Note that $h_{\text{mod_SAR}}$ represents total freeboard relative to the water surface retrieved from the pixel at 10×10 m spacing size. The retrieved sea ice elevations DEMs are compared with h_{DMS} over the testing set, shown in Fig. 6(b). The RMSE between $h_{\text{mod_SAR}}$ and h_{DMS} is 0.26 m. This result is promising as Dierking et al. (2017) suggested the satisfactory accuracy for a

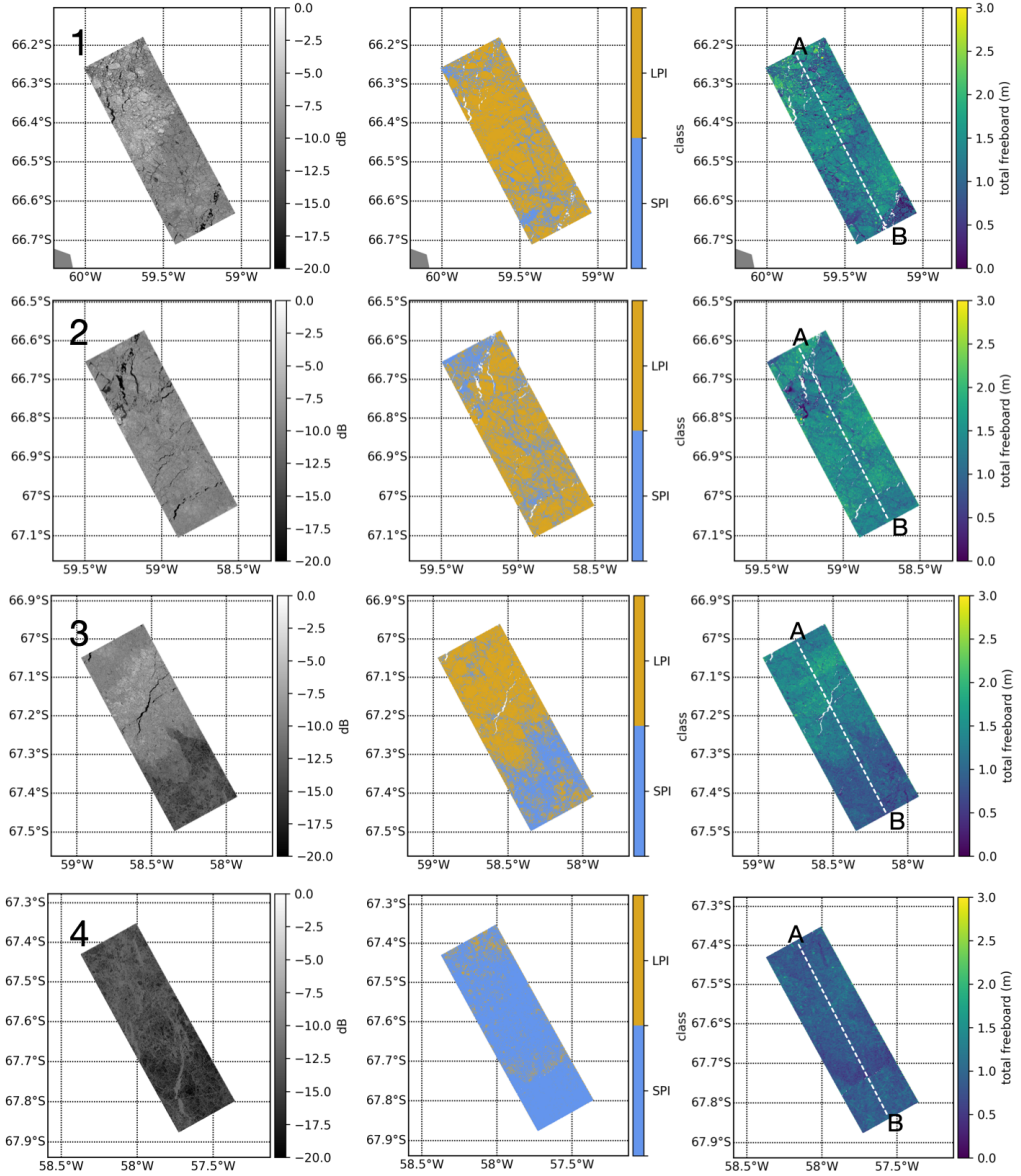


Figure 5. (a) First column: SAR backscattering intensity in HH polarization; (b) Second column: sea ice classification; and (c) Third column: sea ice DEM ($h_{\text{mod_SAR}}$) over the four scenarios. Each row corresponds to Scene No. 1-4 in Fig. 2, respectively. The white dashed line indicates void pixels in the flight track overlapped by the DEM DEM (h_{DMS}) second and third columns represent water areas excluded from processing due to $\text{TaSAR} < 0.3$.

The white dashed line indicates the flight track overlapped by the DEM DEM (h_{DMS}).

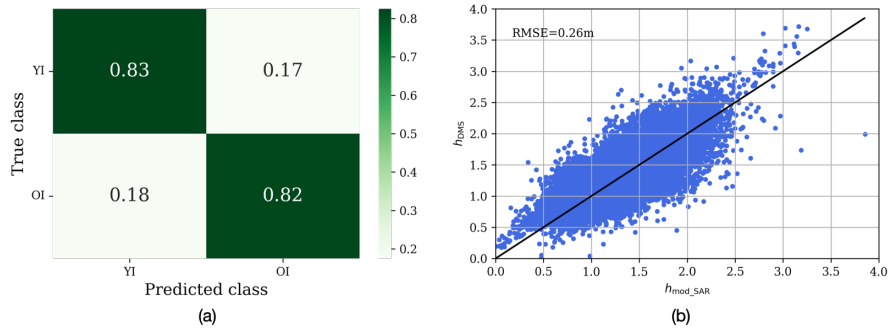


Figure 6. (a) Confusion matrix for sea ice classification. (b) Comparison between the reference height and the derived height over ~~OF-LPI~~ and ~~YISPI~~.

300 sea ice DEM being less than 0.3m. Note that the average RMSE value of LPI without compensating the penetration bias is $\sim 1.10\text{m}$ (Huang et al., 2021).

The $h_{\text{mod_SAR}}$ over the entire SAR images are displayed in the right column of Fig. 5. For each scene, the white dash line delineates a $50\text{ km} \times 100\text{ m}$ strip overlapped with DMS DEM. By extracting the values at the center of the strip, the height profiles are presented in Fig. 7, where $h_{\text{mod_SAR}}$ performs good agreement with the reference data (h_{DMS}) and well capture the 305 topographic variation. Considering that h_{DMS} already contains an uncertainty of 0.2m (Dotson and Arvesen., 2012, updated 2014), these results prove the effectiveness of the proposed two-step approach for sea ice DEM retrieval over both ~~YI and OI~~ and ~~LPI~~.

4.2 Sea ice topography along the southwards direction

We obtain sea ice DEM over the total 162 images using the two-step approach, shown in. A visualization of the derived sea 310 ice DEM can be found in the appendix Fig. ??A5 and A6. The derived DEM is downsampled to a resolution of 500m, utilized in the subsequent analyses.

The northernmost location on each segment is selected and marked with star symbol in Fig. ??1. Subsequently, we characterize the variation of sea ice category, elevation total freeboard, and roughness moving southward, using distances relative to the northernmost locations and averaging over every 100km interval. These topographic variations along the distance are 315 illustrated in Fig. 8- 10.

The first column shows the OF-LPI percentages estimated from the proposed two-step approach and compared with the Ice Charts. The overall trend of estimated LPI percentages correlates well with dominant ice types and ice concentrations from the Ice Charts across most segments (W1-U, W1-L, which are used as the reference. For instance, the average ice type of the W2-U, W4, W5-U, W5-L, and R5). Specifically, W1-U segment is MYI within the 0–160 km range, matching the estimated around and W1-L are explained as two examples. W1-U from 0–120 km is covered by 100% MYI, where the LPI percentage reaches its highest value (58% OI from our method. FYI becomes dominant from 160–320 km, aligning with

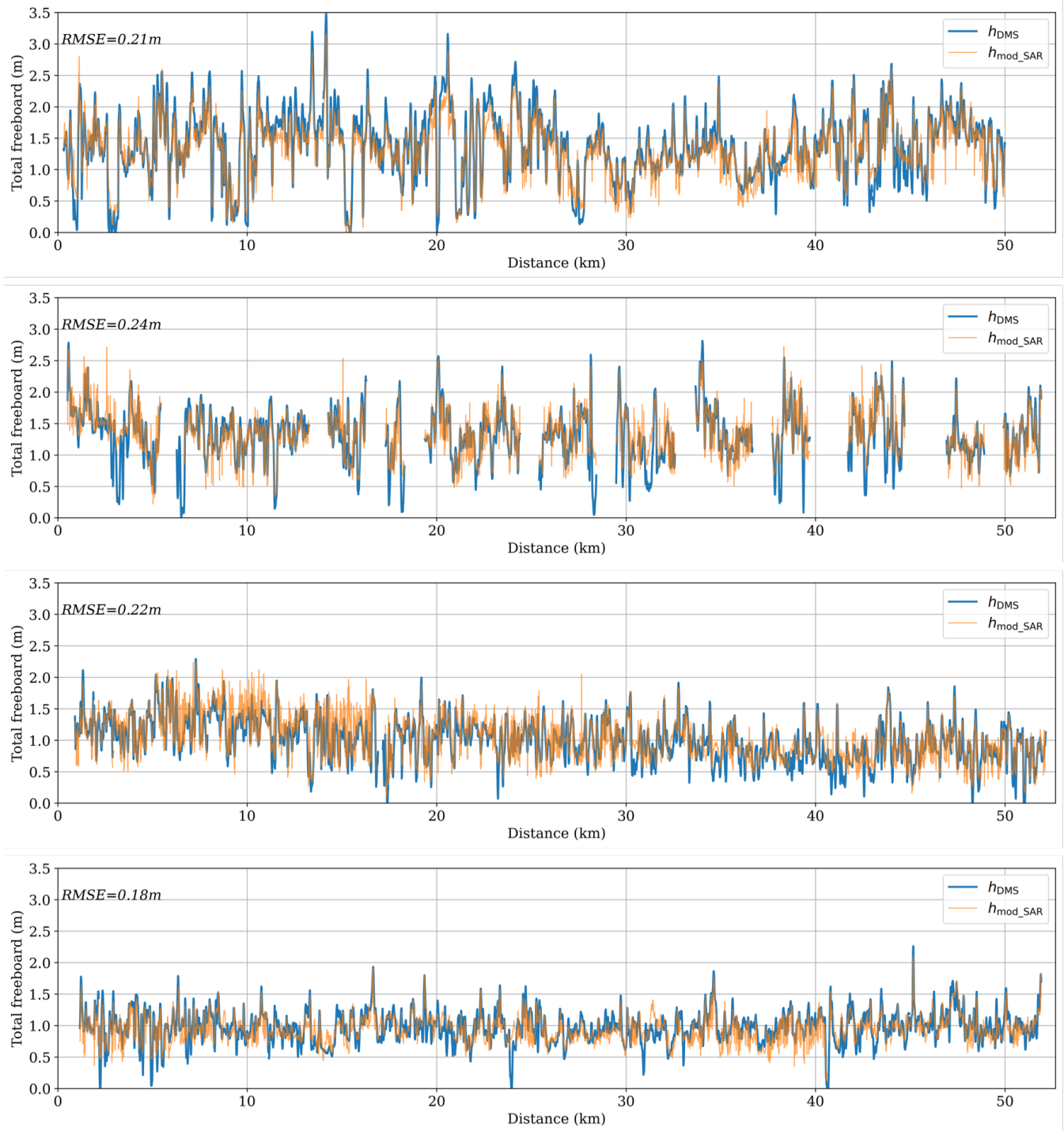


Figure 7. Comparison between the [elevation-total freeboard](#) profiles (h_{mod_SAR}) from the proposed method and the DMS DEM (h_{DMS}) along the dotted line (from A to B) over Scene No.1-4 in Fig. 5(c). [The data gaps are the water areas and segments that were excluded due to the absence of distinctive features, ensuring co-registration quality.](#)

325 a decrease in OI percentage). As the dominant ice transitions from MYI to FYI from 120 – 400 km, the LPI percentage decreases accordingly. The dominance of MYI ice from 400 – 600 km also corresponds to the increasing LPI percentage. For W1-L, where the distance between 500 – 600 km is covered by 100% MYI, and the LPI percentage peaks before decreasing after 650 km distance as FYI becomes dominant. The lowest LPI percentage is found around 1200 km, consistent with the occurrence of TI at this distance. Beyond 320 km, MYI dominates again, consistent with an increase in the estimated OI percentage.

330 The overall trend of estimated OI percentages aligns well with the Ice Charts across most segments (W1-U, W1-L, W2-U, W4, W5-U, W5-L, and R5). For other segments observed similar trend can be explained by the general assumption that MYI is thicker and less saline, allowing for deeper radar penetration compared to FYI and TI. However, penetration depth is influenced by various factors not only ice age, but also ice salinity, snow condition, flooding effects, and temperature. This explains the discrepancies for other segments (W2-L, W3-U, W3-L, some discrepancies exist, which can R1-U, R1-L). Furthermore, discrepancies can also be attributed to the differences in spatial resolution and temporal gap between the gaps between Ice Charts and SAR imagery, considering the dynamic nature of sea ice. It should be emphasized that the proposed method classifies ice based on electromagnetic wave penetration into snow and ice, which may have differences when compared with the conventional ice types in Ice Charts.

335 It is essential to clarify that we utilized Ice Charts data as external information to interpret the classification results and spatial variation of topography. However, we did not use Ice Charts to quantitatively validate the proposed method. For validation purposes, we conducted pixel-by-pixel comparisons using co-registered DMS data.

340 The second and third columns in Fig. 8-10 display the distance dependency of ice elevation ($h_{\text{mod,SAR}}$) total freeboard ($h_{\text{mod,SAR}}$) and roughness (σ_R), respectively. Sea ice roughness is the standard deviation of the elevation total freeboard within a 50×50 m area. For each 100 km-distance interval, we calculate and display the average and median values, as well as the first and third quartiles of $h_{\text{mod,SAR}}$, $h_{\text{mod,SAR}}$ and σ_R using boxplots.

345 Sea ice DEM ($h_{\text{mod,SAR}}$) over (a) the Weddell Sea and (b) the Ross Sea retrieved from SAR images. The northernmost locations on each segment are marked with star symbols and serve as reference points for calculating the relative distance.

350 The Ice Charts are also used to validate and explain the topographic variation of sea ice. In general, the region with thicker ice (e.g., MYI) is anticipated to display higher elevation total freeboard or larger roughness compared to the area with thinner ice, such as FYI and TI. This hypothesis is substantiated by the agreement between topographical variations (elevation total freeboard and roughness) and ice types observed in Fig. 8 to 10 across most segments, with the exception of W3-L and W5-L. The sea ice is identified as MYI between 450 – 750 km in W3-L and 650 – 1000 km in W5-L. However, neither elevation total freeboard nor roughness significantly increases within these specific ranges. Minor discrepancies also persist, for instance, in W1-U and W2-L, where there is no clear reduction in either elevation total freeboard or roughness when FYI is present at around 600 km. Considering These discrepancies may arise due to the local cases where rough FYI exhibits greater roughness than smooth level MYI. FYI may also show higher elevations when covered by very thick snow. In addition, 355 considering that the Ice Charts data are weekly average products, the inconsistencies could be attributed to mis-coregistration caused by sea ice drift during the time lag between the Ice Charts data and the SAR images.

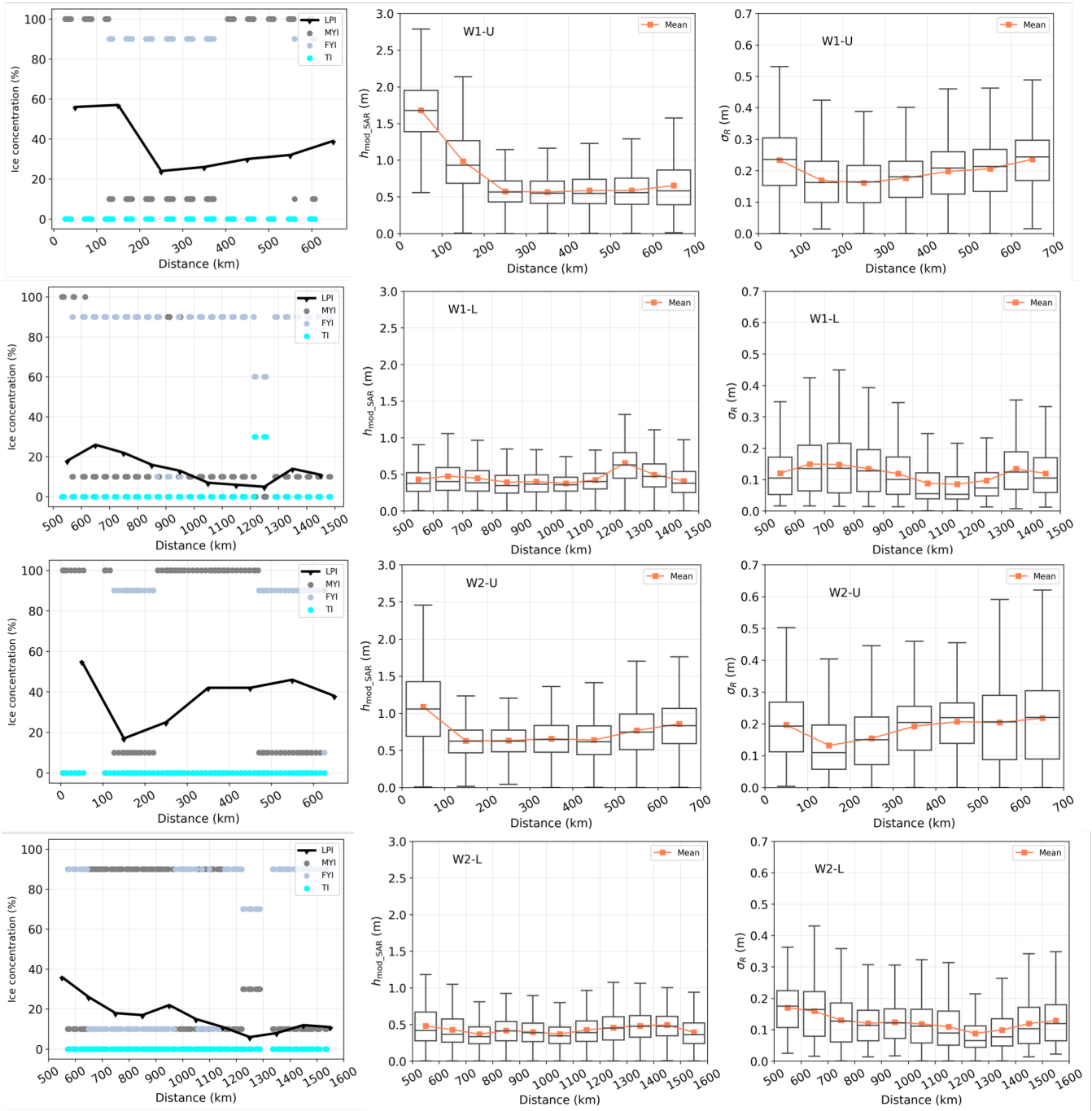


Figure 8. Sea ice characteristics along the southwards direction along W1 and W2 segments. The blue line in the first column displays the OI-LPI percentages derived from SAR images, and the blue dot indicates the ice types obtained from the Ice Charts. The second and third columns plot the $\text{elevation-total freeboard}$ ($h_{\text{mod,SAR}}$) and roughness (σ_R), respectively. Distance is measured from the northernmost SAR image reference point towards the south. The orange line denotes the average values of $h_{\text{mod,SAR}}$ and σ_R . The box's upper and lower boundaries represent the first (Q1) and third (Q3) quartiles, while the upper (lower) whisker extends to the last (first) sample outside of $Q3 \pm 1.5 \times (Q3 - Q1)$.

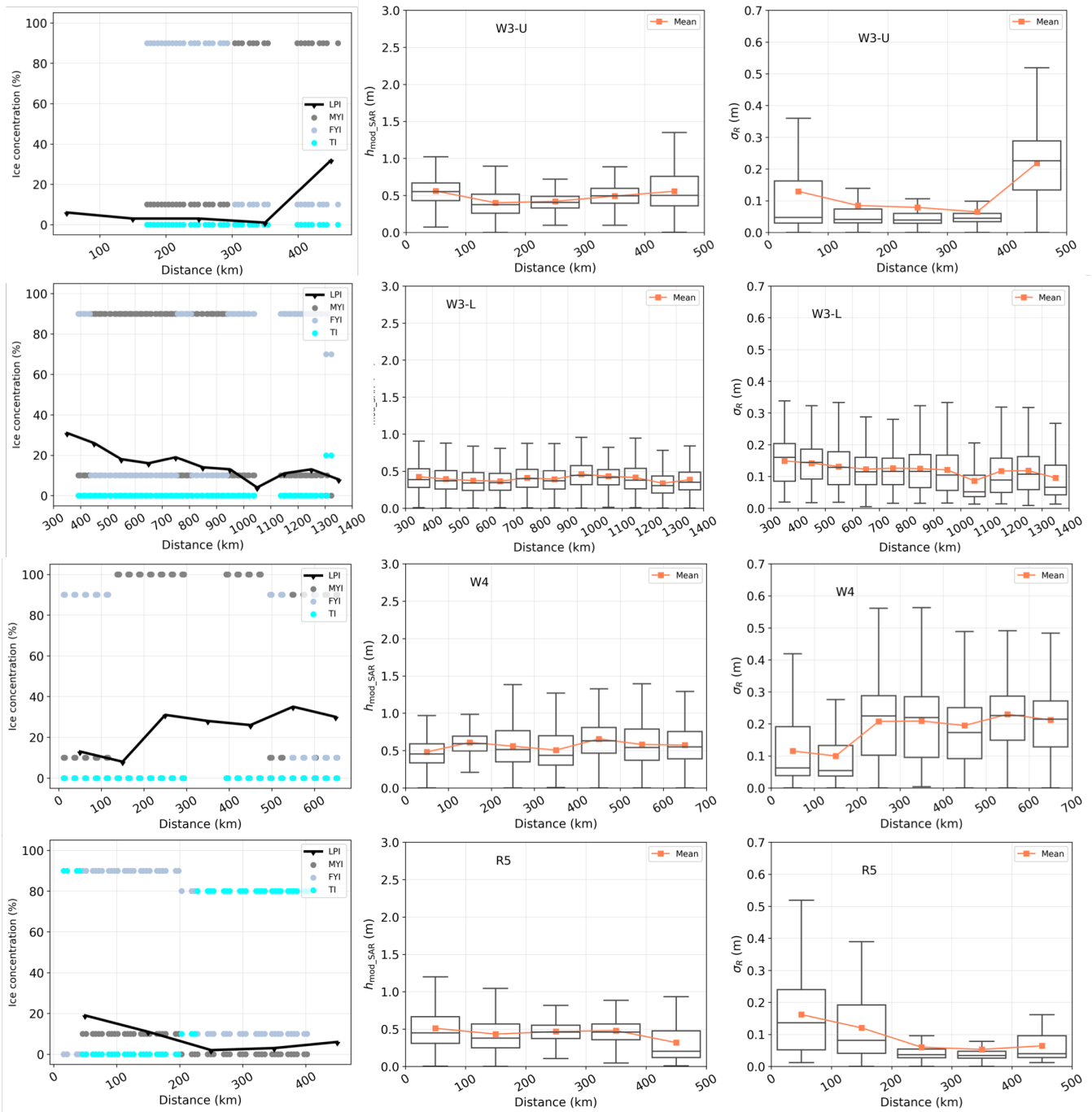


Figure 9. Sea ice characteristics along the southwards direction along W3, W4, and R5 segments. The blue line in the first column displays the OLPI percentages derived from SAR images, and the blue dot indicates the ice types obtained from the Ice Charts. The second and third columns plot the elevation-total freeboard ($h_{\text{mod_SAR}}$) and roughness (σ_R), respectively.

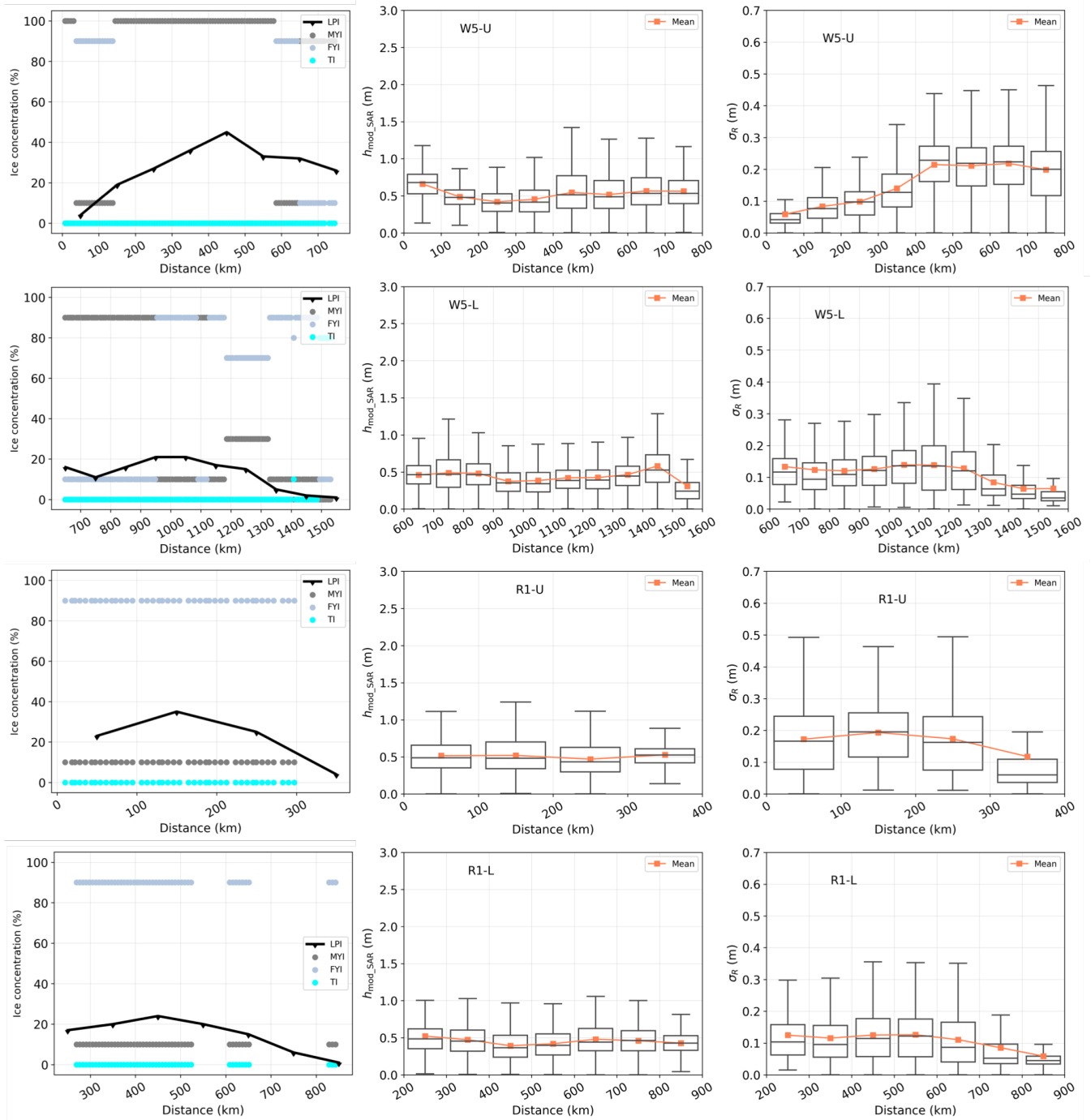


Figure 10. Sea ice characteristics along the southwards direction along W5 and R1 segments. The blue line in the first column displays the OLPI percentages derived from SAR images, and the blue dot indicates the ice types obtained from the Ice Charts. The second and third columns plot the elevation-total freeboard ($h_{\text{mod,SAR}}$) and roughness (σ_R), respectively.

In the northwestern Weddell Sea, we observe that the sea ice near the Antarctic Peninsula (AP) in the W1-U and W2-U segments exhibits the highest average ~~elevation~~^{total} freeboard (mean > 0.7 m) and roughness (mean 0.19m) shown in the first and third rows in Fig. 8. This observation aligns with a previous study using OIB Airborne Topographic Mapper (ATM) data from November 14 and 22, 2017 (Wang et al., 2020), which has reported that the ~~snow~~^{total} freeboard near the eastern AP ranges from 1.5 – 2.5 m. Moving outwards from the AP, the ~~sea-ice~~^{elevation}~~total~~ freeboard and roughness along W1-U and W2-U demonstrate a sharp decrease within approximately 0 – 200 km before gradually increasing as it heads southward. Similar trends are observed in W3-U (first row in Fig. 9) and W5-U (first row in Fig. 10), with a more subtle decrease in ~~elevation and roughness~~^{total} freeboard within the 0 – 200 km range, compared to W1-U and W2-U, followed by a southward increase. Conversely, in the initial 0 – 200 km of W4 (third row in Fig. 9), there's no observed decrease in ~~elevation~~^{total} freeboard or roughness. Instead, a gradual increase in both parameters is evident as one moves southward, consistent with the dominance of MYI beyond 100 km from the Ice Charts data. In the southeastern region, segments W1-L, W2-L, W3-L, and W5-L exhibit similar patterns in the topographic variation, with ~~elevation~~^{total} freeboard and roughness generally decreasing towards the south as they approach the Coats Land ~~-(see location in Fig. 1)~~. This trend can be explained by the increasing occurrence of FYI or TI beyond ~~~1200km~~^{around 1000 km} from the Ice Charts data.

The observed variation in sea ice topography can result from the formation and dynamics of sea ice in the East Weddell (E-Wedd) and West Weddell (W-Wedd) regions, which are defined by specific longitude ranges: E-Wedd encompasses 15°E to 40°W, while W-Wedd extends from 40°W to 62°W. Segments of W1-U, W2-U, W3-U, W4, and W5-U are located within the W-Wedd, which has been reported for the presence of MYI in the Antarctic (Lange and Eicken, 1991). Sea ice initially forms in the eastern region and then circulates clockwise within the cyclonic gyre of the southern Weddell Sea. Later, older sea ice drifts outward northwestern (Kacimi and Kwok, 2020). The sea ice undergoes thickening and deformation as it drifts (Vernet et al., 2019; Kacimi and Kwok, 2020), resulting in increased ~~elevation~~^{total} freeboard and greater roughness in the northwestern Weddell Sea.

In the Western Ross Sea, the sea ice ~~in~~^{along} the R5 segment (last row in Fig. 9) exhibits greater ~~elevation~~^{total} freeboard and roughness near Terra Nova Bay ~~(see Fig. 1 for the location)~~, with decreasing southeastward. This observation aligns with the ~~evolution of transition of dominant~~ ice types from ~~MTI~~^{FYI} to TI in that direction. This observation is also consistent with recent research (Rack et al., 2021), where airborne measurements in November 2017 revealed deformed sea ice exceeding 10 m in thickness within the first 100 km south of Terra Nova Bay, and thinner ice was observed towards the southeastern area near McMurdo Sound (see Fig. ~~??b-1~~ for the location). Satellite data also confirmed a region of thinner ice influenced by the Ross Sea Polynya, with thicker ice located westward (Kurtz and Markus, 2012). The observed pattern can be attributed to significant deformation in the Western Ross Sea caused by wind-driven shearing, rafting, and ridging within a convergent sea ice regime (Hollands and Dierking, 2016). This deformation leads to potentially thicker sea ice compared to the eastern part (Rack et al., 2021).

For the R1 segment located in the Eastern Ross Sea (third and fourth rows in Fig. 10), although the sea ice exhibits relatively stable ~~elevation~~^{total} freeboard, which agrees with the consistent presence of predominantly FYI, the roughness decreases towards the southeastern. This may be attributed to the influence of ocean circulation, considering that the R1 segment is

situated farther from the land than the other segments. The variation of the roughness along the R1 segment ~~also highlights the importance of combining topographic mapping with ice category mapping to comprehensively characterize sea ice features. suggests that ice topography provides add-on information that can be useful to be integrated into the operational ice charting.~~ Furthermore, Since the edges of ice floes with open water between the floes can also contribute to the ice roughness, combining ice topography with ice concentration can help characterize the sea ice more comprehensively.

4.3 Regional variation of sea ice topography

Figure 11(a) displays the topographic variation across different segments. We present the average and median values, as well as the first and third quartiles of ~~elevation~~total freeboard and roughness using boxplots. The mean values are listed in Table 3. Additionally, the percentages of the three ice types within each segment, calculated from the Ice Charts for reference, are presented in Fig. 11(b).

Generally, sea ice in the northwestern Weddell Sea (W1-U, W2-U, W3-U, W4, W5-U) exhibits higher average ~~elevations~~total freeboard (> 0.5 m) compared to that in the southeastern Weddell Sea and the Ross Sea (W1-L, W2-L, W3-L, W5-L, R1-U, R1-L, R5), see detailed values in Table 3. W1-U and W2-U exhibit the highest average ~~elevations~~total freeboard of 0.8 m and 0.72 m, respectively, along with the largest average roughness of 0.19 m. This is comparable with the ~~snow~~total freeboard retrieved from ICESat-2 (Kacimi and Kwok, 2020), reporting an average of 0.6 – 0.7 m ~~snow~~total freeboard nearby the Eastern AP between April 1 and November 16, 2019. W4 and W5-U show average ~~elevations~~total freeboard of 0.57 m and 0.52 m, and average roughness values of 0.18 m and 0.16 m, respectively. The above topographic values (i.e., ~~elevation~~total freeboard and roughness) are consistent with the ice types presented in Fig. 11(b), where W1-U, W2-U, W4, and W5-U exhibit a substantial proportion ($\geq 57\%$) of MYI, known for greater ~~elevation~~total freeboard and roughness characteristics. W3-U, which consists of 47% MYI, exhibits ~~an elevation a~~total freeboard of 0.50 m but with relatively lower roughness at 0.11 m, suggesting the possibility of a smooth snow-air interface over older and thicker ice.

For the segments in the southeastern Weddell Sea and the Ross Sea (W1-L, W2-L, W3-L, W5-L, R1-L, and R5), the average ~~sea ice elevation~~total freeboard remains below 0.46 m and roughness around 0.11 m. The reduced average ~~elevation~~total freeboard and roughness correspond to ice types with fewer MYI percentages ($\leftarrow 50\% \leq 52\%$) and greater amounts of FYI and TI ($\rightarrow 50\% > 52\%$). R1-U demonstrates an average ~~sea ice elevation~~total freeboard of 0.49 m and roughness of 0.18 m, with the presence of predominantly FYI throughout the region. This observation suggests a plausible scenario of a rougher snow-air interface over younger and thinner ice (Tin and Jeffries, 2001; Tian et al., 2020).

4.4 Statistical analyses of sea ice topography

Studies on sea ice topography in the Arctic have extensively examined the applicability of statistical distributions such as the log-normal distribution (Landy et al., 2020; Duncan and Farrell, 2022) and the exponentially modified normal (exp-normal) distribution (Yi et al., 2022). However, there remains a gap in understanding the most suitable distribution models for describing the ~~elevation~~total freeboard of Antarctic sea ice. We aim to address this gap by evaluating three distribution models: Gaussian,

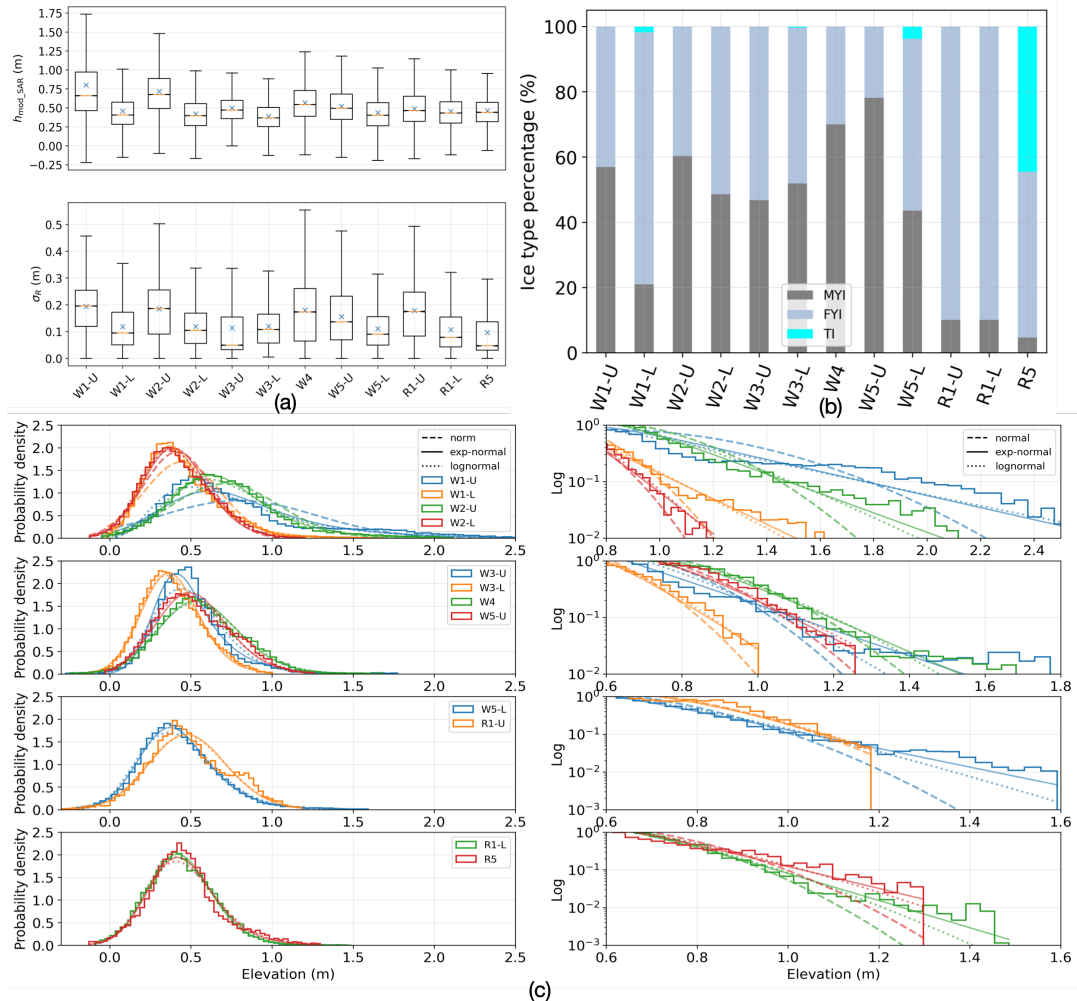


Figure 11. (a) Sea-ice elevation Total freeboard ($h_{\text{mod_SAR}}$) and roughness (σ_R) derived from SAR images across the 12 segments. (b) The percentage of multi-year ice (MYI), first-year ice (FYI), and thin ice (TI) from the Ice Charts. (c) Probability density function (PDF) of derived sea-ice elevation total freeboard ($h_{\text{mod_SAR}}$) and their fits to the exponential-normal, log-normal, and normal distributions.

Table 3. Average elevation-total freeboard and roughness for each segment, as well as the Kolmogorov-Smirnov (KS) values between the observed elevations-total freeboard and modeled distributions (i.e., exponential normal and log-normal). The smaller KS value is in **bold**.

segment	Mean <u>elevation-total freeboard</u> (m)	Mean roughness (m)	KS exp-normal	KS log-normal
W1-U	0.80	0.19	0.083	0.106
W1-L	0.46	0.12	0.064	0.05
W2-U	0.72	0.19	0.052	0.07
W2-L	0.42	0.12	0.079	0.054
W3-U	0.50	0.11	0.113	0.2
W3-L	0.39	0.12	0.065	0.05
W4	0.57	0.18	0.035	0.072
W5-U	0.52	0.16	0.074	0.076
W5-L	0.44	0.11	0.038	0.078
R1-U	0.49	0.18	0.053	0.049
R1-L	0.45	0.11	0.049	0.106
R5	0.46	0.10	0.052	0.039
Overall			0.063	0.079

log-normal, and exp-normal, to determine the most appropriate probability density function (PDF) for describing the sea-ice 425 elevation-total freeboard across segments.

The PDF of the Gaussian distribution with mean μ_g and standard deviation σ_g is defined as:

$$G(x) = \frac{1}{\sqrt{2\pi\sigma_g^2}} e^{-\frac{(x-\mu_g)^2}{2\sigma_g^2}} \quad (10)$$

The PDF of the log-normal distribution with mean $e^{(\mu_l+\sigma_l^2/2)}$ and variance $e^{2\mu_l+\sigma_l^2} (e^{\sigma_l^2} - 1)$ follows (Gaddum, 1945):

$$LG(x) = \frac{1}{x\sigma_l\sqrt{2\pi}} e^{-\frac{(\ln(x)-\mu_l)^2}{2\sigma_l^2}} \quad (11)$$

430 The PDF of the exp-normal distribution with mean $\mu_e + 1/\lambda$ and variance $\sigma_e^2 + 1/\lambda^2$ is given as (Foley and Dorsey, 1984):

$$EMG(x) = \frac{\lambda}{2} e^{\frac{\lambda}{2}(2\mu_e + \lambda\sigma_e^2 - 2x)} \operatorname{erfc}\left(\frac{\mu_e + \lambda\sigma_e^2 - x}{\sqrt{2}\sigma_e}\right) \quad (12)$$

where the $\operatorname{erfc}(\cdot)$ is the complementary error function with $\operatorname{erfc}(x) = \frac{2}{\sqrt{\pi}} \int_x^\infty e^{-t^2} dt$.

The observed and modeled distributions of sea ice-elevation-total freeboard over each segment are depicted in the left column 435 of Fig. 11(c). The observed distributions of all segments exhibit asymmetrical with longer tails. A closer examination of the tail regions (right column in Fig. 11(c)) reveals significant deviations from the Gaussian distribution, particularly in segments

W1-U and W2-U, which are covered by deformed and thicker sea ice. The observed non-Gaussian nature of ~~sea ice elevation~~ ~~total freeboard~~ distribution aligns with the previous studies (Hughes, 1991; Davis and Wadhams, 1995; Castellani et al., 2014; Landy et al., 2019; Huang et al., 2021). To quantitatively evaluate the fit of non-Gaussian distributions (i.e., log-normal and exp-normal) to the observed ~~elevations~~ ~~total freeboard~~, we employ the Kolmogorov-Smirnov (KS) test (Massey Jr, 1951). This 440 test measures the goodness of fitting by calculating the distance between the observed distribution function and the theoretical cumulative distribution function. The values of the KS test are given in Table 3, where a lower value indicates a better fit.

In the northwestern Weddell Sea, where the segments (W1-U, W2-U, W3-U, W4-U, and W5-U) have average ~~elevations~~ ~~total freeboard~~ greater than 0.5 m, the exp-normal distribution demonstrates superior fitting performance, as evidenced by smaller KS values. This can be attributed to the exp-normal distribution's incorporation of an exponential component, which enables a 445 better fit to data with heavy or long tails compared to the log-normal distribution. Consequently, the exp-normal distribution is better suited for characterizing the statistics of older and thicker sea ice, which often involves strong deformation and exhibits significant ~~elevations~~ ~~total freeboard~~.

In the southern Weddell Sea and the Ross Sea, segments average below 0.5 m in ~~elevation~~ ~~total freeboard~~, with varying fits between exp-normal and log-normal distributions. The log-normal distribution exhibits a better fit for W1-L, W2-L, W3-L, 450 R1-U, and R5, while the exp-normal distribution is more appropriate for W5-L and R1-L. This observation suggests that the two distributions perform comparably in characterizing the ~~elevations~~ ~~total freeboard~~ of younger and thinner sea ice.

Evaluating the overall performance across all segments, the exp-normal distribution outperforms the log-normal distribution, as indicated by a smaller average KS value of 0.063.

5 Discussion

455 5.1 Factors affecting the model performance

In the proposed two-step method (Fig 3), we obtain snow depth from the AMSR products (Meier et al., 2018), which represents a five-day running average of snow depth over sea ice. Due to the limited spatial (12.5 km) and temporal resolution in the snow depth data, we assume a constant value of snow depth across one SAR image. Hence, for each SAR acquisition covering a spatial extent of 50×19 km, we compute the mean snow depth and utilize it as input parameter z_1 in the TLPV model.

460 In Fig. 7, it appears the derived total freeboard ($h_{\text{mod_SAR}}$) underestimates some high and low peaks of the reference data (h_{DMS}). One factor contributing to the underestimation of total freeboard could be the assumption of a constant average snow depth over one SAR scene. Using a single average value of snow depth may lead to an underestimation of snow depth in high-peak areas such as ridges, consequently resulting in an underestimation of the total freeboard. Our prior study (Huang et al., 2021) demonstrated a mean difference of 0.31 m in the derived total freeboard due to snow depth variations from 465 0.05 to 0.75 m over Scene No.1, highlighting the impact on peak estimation. In the future, it would be interesting to adapt the proposed method over the test sites co-locating with available high-resolution snow depth measurements.

Another factor that could potentially lead to the underestimation of high and low peaks is the residual shift between the SAR and DMS images. Although we carefully co-registered the four SAR scenes with the DMS data, the co-registration can not be

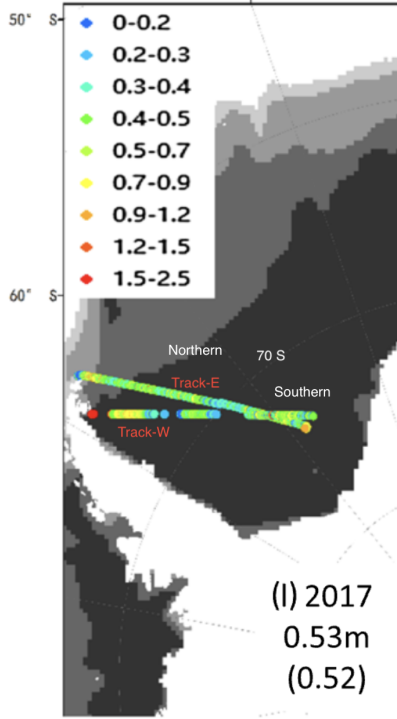


Figure 12. The total freeboard calculated from IceBridge Laser Altimetry (copy of Fig.61 by Wang et al. (2020)). We labeled the two tracks Track-W and Track-E. The region with latitude $< 70^{\circ}\text{S}$ ($> 70^{\circ}\text{S}$) is referred to as the northern (southern) track.

perfect. In the process, we divided the entire overlapped transect into small patches (each corresponding to $100 \times 1000\text{ m}$). We 470 assumed the same drift location over one patch and no rotation; thus, only one shift vector was used for co-registration over each patch. This could result in small residual shifts when the ice floes or features do not drift at the same velocity or involve rotations within the patch. The presence of low- and high-peak ice features with narrow sizes spanning just a few pixels, poses a challenge. Even slight residual shifts, as small as 1-2 pixels, can lead to loss or misalignment of peak structures in SAR images. Consequently, these slightly misaligned SAR images input into the proposed model may result in an underestimation 475 of the total freeboard.

5.2 Compare the InSAR-derived total freeboard with existing study

Wang et al. (2020) calculated the mean total freeboard in the Weddell Sea using the IceBridge Laser Altimetry. In this subsection, we conduct a visual comparison between Wang et al. (2020)'s result (Fig. 12) with the four segments (W2-U, W2-L, W3-U, and W3-L) in our study (Fig. 8 and 9). Note that the window size is ten-of-kilometer scales in Wang et al. (2020)'s study, significantly exceeding the $500 \times 500\text{ m}$ window size we used. 480

We denote the region in Fig. 12 with latitude $< 70^{\circ}\text{S}$ ($> 70^{\circ}\text{S}$) as the northern (southern) track. The Northern and Southern Track-W segments are partially overlaid with W2-U and W2-L, respectively. In our study, the total freeboard of W2-U and W2-L in Fig. 8 reaches a mean value of $\sim 1\text{ m}$ and 75% percentile value of $\sim 1.5\text{ m}$ within the first 100 km, which agrees with the red dot in Fig. 12 Track-W. Then, the total freeboard goes down to a mean value as $\sim 0.7\text{ m}$ and 75% percentile value of $\sim 0.75\text{ m}$ from 100 – 200 m. Although there is a data gap in Fig. 12, we can see that color of the dots changes from red to yellow, which is consistent with the decreasing trend of the total freeboard within 300 km from our results. For W2-L, the mean total freeboard from our result is around 0.5 m, agreeing with a mix of green and yellow dots (0.4 – 0.9 m) in the Southern Track-W in Fig. 12. Note that the OIB ATM data in (Wang et al., 2020) was acquired on 14 and 22 November 2017, while the SAR images in our study were acquired on 30 and 25 October 2017 for W2-U and W2-L, respectively. The sea ice drifts and potential melting could induce slight differences between our results and Wang et al. (2020).

The W3-U and W3-L can be compared with Northern and Southern Track-E, respectively. From Fig. 12, a mix of green and yellow dots in the northern Track-E represent the total freeboard 0.5 – 1.2 m, which agrees well with our result for W3-U, see the first row in Fig. 9. At around 70°S , the dots transit to a mix of cyan and blue colors, representing the total freeboard of 0.2 – 0.7 m, which is consistent with the W3-L in Fig. 9. The slight difference can be attributed to the temporal difference of SAR images used in our study. Specifically, the image for W3-L was acquired on 26 October 2017, while the Track-E image was acquired on 22 November 2017.

6 Conclusions

In this study, we proposed a novel two-step approach integrating machine learning and polarimetric-interferometry techniques to retrieve ~~sea ice elevation total freeboard~~ from dual-pol single-pass InSAR images, taking into account the variations in penetration bias over different ice classes. Initially, a random forest classifier was employed to categorize sea ice (i.e., ~~YI and OISPI and LPI~~) based on microwaves' penetration. Subsequently, the standard InSAR processing technique was applied to retrieve the ~~elevation over YI total freeboard over SPI~~ regions, where the penetration depth is negligible. For ~~OI LPI~~ regions, an inversion algorithm for the TLPV model was developed. This algorithm can effectively compensate for the radar penetration bias into snow and ice, achieving an accurate sea ice DEM (i.e., ~~snow total~~ freeboard). ~~Utilizing the OTASC dataset, which spans an area of $200 \times 19\text{ km}$, the efficiency of the proposed method was validated with an RMSE of 0.26 m. The uncertainty level is satisfactory for LPI with RMSE of 0.26 m. However, this accuracy is insufficient for thinner ice whose height above sea level is only tens of centimetres or even less. Given that a substantial portion of Antarctic sea ice consists of first-year ice with a thickness of approximately one meter (Scott, 2023), achieving accurate DEM retrieval over thinner ice remains a challenge. In the future, a potential single-pass InSAR configuration using a higher frequency, such as Ku-band, along with a longer cross-track baseline, would result in a smaller height of ambiguity (HoA) of less than 5 m (López-Dekker et al., 2011). This setup can enhance InSAR sensitivity and improve the accuracy of total freeboard measurements.~~

The proposed approach was applied to a broad area in Antarctica. Overall, sea ice in the northwestern Weddell Sea exhibits higher average ~~elevations total freeboard~~ ($> 0.5\text{ m}$) than the southeastern region and the Ross Sea, where the average ~~elevations~~

515 ~~are total freeboard is~~ lower (< 0.5 m). In the northwestern Weddell Sea, sea ice experiences substantial deformation near the eastern AP, followed by a pronounced decline in both ~~elevation total freeboard~~ and roughness within a range of 0 – 200 km. Subsequently, there is a gradual increase in these parameters as one moves southward. In the southeastern Weddell Sea, the ~~sea ice elevation total freeboard~~ and roughness generally decrease towards the south as they approach Coats Land. In the Western Ross Sea, thicker and rougher ice was observed near Terra Nova Bay, while thinner ice was found in the southeastern area near McMurdo Sound. In the Eastern Ross Sea, the stable ~~sea ice elevation total freeboard~~ aligns with the prevalent presence of 520 FYI, but roughness decreases towards the southeastern. These findings emphasize that topographic mapping can enhance ice category delineation, providing an in-depth understanding of sea ice characteristics.

Furthermore, the statistical analyses of ~~sea ice elevation total freeboard~~ confirmed its non-Gaussian distribution. The results further suggested that the exp-normal distribution outperforms the log-normal distribution in fitting the ~~elevations total freeboards~~ of regions with an average ~~elevation total freeboard~~ greater than 0.5 m, particularly for older and thicker sea ice, 525 whereas both distributions perform comparably for regions with an average ~~elevation total freeboard~~ lower than 0.5 m.

530 ~~Future studies~~ The spatial distribution of penetration depth (total freeboard minus radar freeboard) can be an interesting topic for future research. In snow-covered sea ice, penetration is significantly influenced by local snow conditions. Hence, conducting a coordinated campaign encompassing TanDEM-X acquisitions, lidar measurements, and in-situ snow assessments holds great promise for analyzing the relation between radar freeboard and total freeboard across different snow conditions. ~~Future studies also~~ involve linking the derived sea ice topographic characteristics associated with oceanographic factors (ocean current and bathymetry) and climatology parameters (wind and temperature). We aim to further advance our comprehension of sea ice dynamics and evolution in Antarctica.

Appendix A: Further details of data processing and figures

A1 InSAR height uncertainty across various height of ambiguity values

535 The HoA (h_a) is the height of ambiguity determined by the specific InSAR configuration such as the radar wavelength, orbit height, incidence angle, and baseline. A larger HoA will elevate the uncertainty in the InSAR-derived height. This uncertainty (σ_h) can be estimated by (Madsen, 1998)

$$\sigma_h = \frac{h_a}{2\pi} \sigma_{\Delta_\phi}$$

540 where σ_{Δ_ϕ} is the phase noise, which can be expressed as a function of the interferometric coherence (γ_{InSAR}) and the independent number of looks (N_L) (Rosen et al., 2000)

$$\sigma_{\Delta_\phi}^2 = \frac{1}{2N_L} \frac{1 - \gamma_{\text{InSAR}}^2}{\gamma_{\text{InSAR}}^2}$$

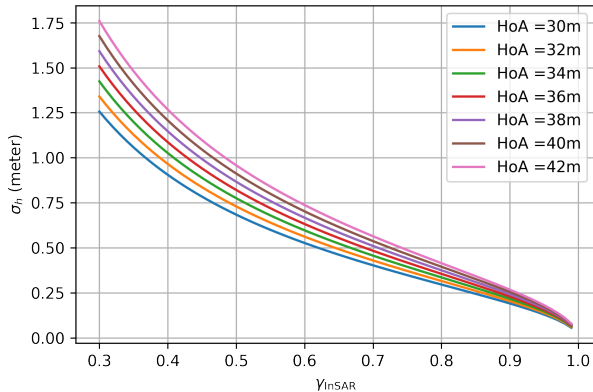


Figure A1. Simulation of σ_h to the variations in h_a and γ_{InSAR} with N_L set to be 73.

The simulated σ_h to the variations in h_a and γ_{InSAR} is illustrated in Fig. A1. At the $\gamma_{\text{InSAR}} = 0.75$, σ_h increases from 0.35 m to 0.48 m corresponding to h_a ranging from 30 m to 42 m. Across the studied region, both the mean and median values of γ_{InSAR} are around 0.75. Consequently, in the case of R5, the larger h_a induces a relatively larger average uncertainty in the derived InSAR height (h_{InSAR}) compared to the smaller h_a InSAR configuration in our dataset.

545

A2 SAR thermal noise removal

The SAR-measured backscattering intensity (σ_{measure}) containing additive thermal noise can be denoted as

$$\sigma_{\text{measure}} = \langle (S_{\text{denoised}} + N) \times (S_{\text{denoised}} + N)^* \rangle \quad (\text{A1})$$

where S_{denoised} is the noise-subtracted backscattering amplitude, and N is the additive thermal noise. Considering S_{denoised} and N to be uncorrelated, the noise-subtracted backscattering intensity can be obtained from the following simple equation (Nghiem et al., 1995)

$$\sigma_{\text{denoised}} = \sigma_{\text{measure}} - NESZ \quad (\text{A2})$$

where $NE SZ$ is the noise floor (i.e., the noise equivalent sigma zero (NE SZ)), and all terms are in the linear scale.

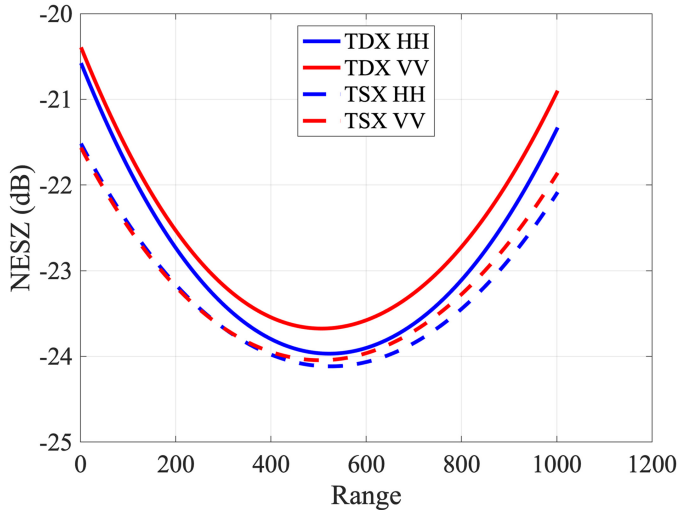


Figure A2. NESZ patterns for one TanDEM-X acquisition (Scene No.1 in Fig. 2) as an example.

The TanDEM-X product contains a set of polynomial coefficients that describe the NESZ pattern for each polarization along the range direction (Eineder et al., 2008) for both the TanDEM-X (TDX) and TerraSAR-X (TSX) images. An example of the calculated *NE SZ* is shown in Fig. A2 in dB scale. By converting to the linear scale, the σ_{denoised} can be calculated by subtracting *NE SZ* from the σ_{measure} . We calculate the *NE SZ* pattern for each SAR acquisition and employ Eq. A2 to generate denoised backscattering intensities for the different polarizations (i.e., HH, VV, Pauli-1 (HH+VV), and Pauli-2 (HH-VV)) from the TSX image. Note that for Pauli-1 and Pauli-2, we use the average *NE SZ* between HH and VV channels.

560 A3 Ranking of SAR features

The Gini importance computed from the Random Forest (RF) classifier is given in Fig A3.

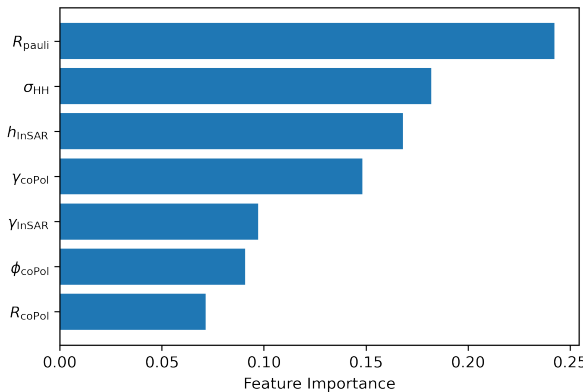


Figure A3. Gini importance computed from the Random Forest (RF) classifier.

The Gini importance computed from the Random Forest (RF) regressor for estimating m and h_v is given in Fig A4.

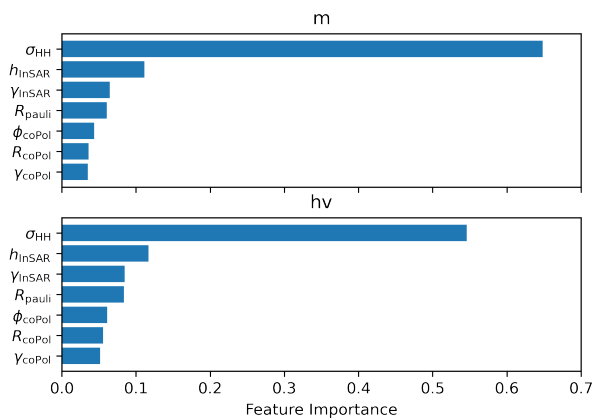


Figure A4. Gini importance computed from the Random Forest (RF) regressor for estimating m and h_v .

A4 Overview of the InSAR-derived total freeboard

The derived total freeboard over the Weddell and Ross Seas are given in Fig. A5 and A6.

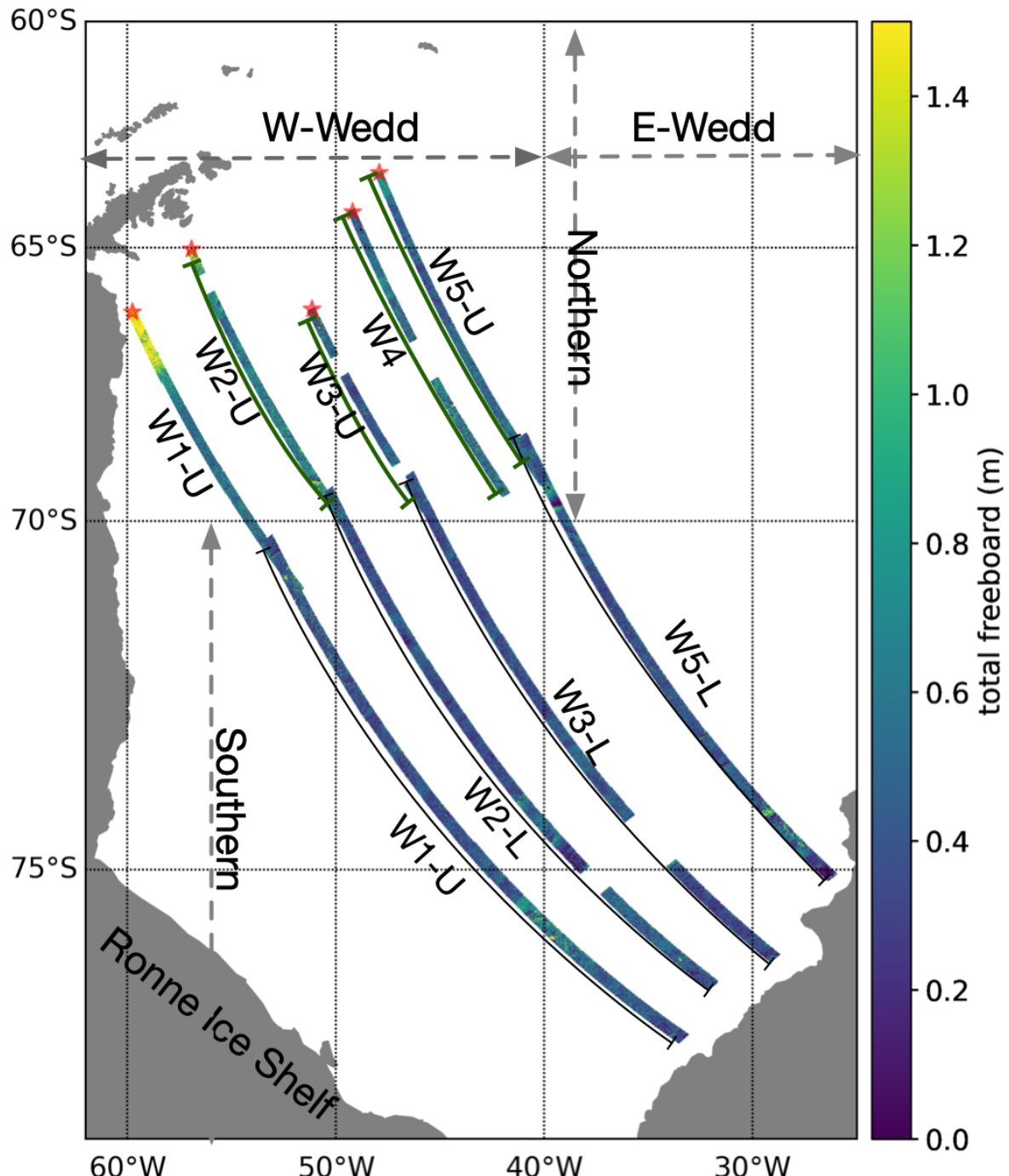


Figure A5. Sea ice DEM ($h_{\text{mod, SAR}}$) over the Weddell Sea retrieved from SAR images. The northernmost locations on each segment are marked with star symbols and serve as reference points for calculating the relative distance. $h_{\text{mod, SAR}}$ was downsampled to 500 m pixel size.

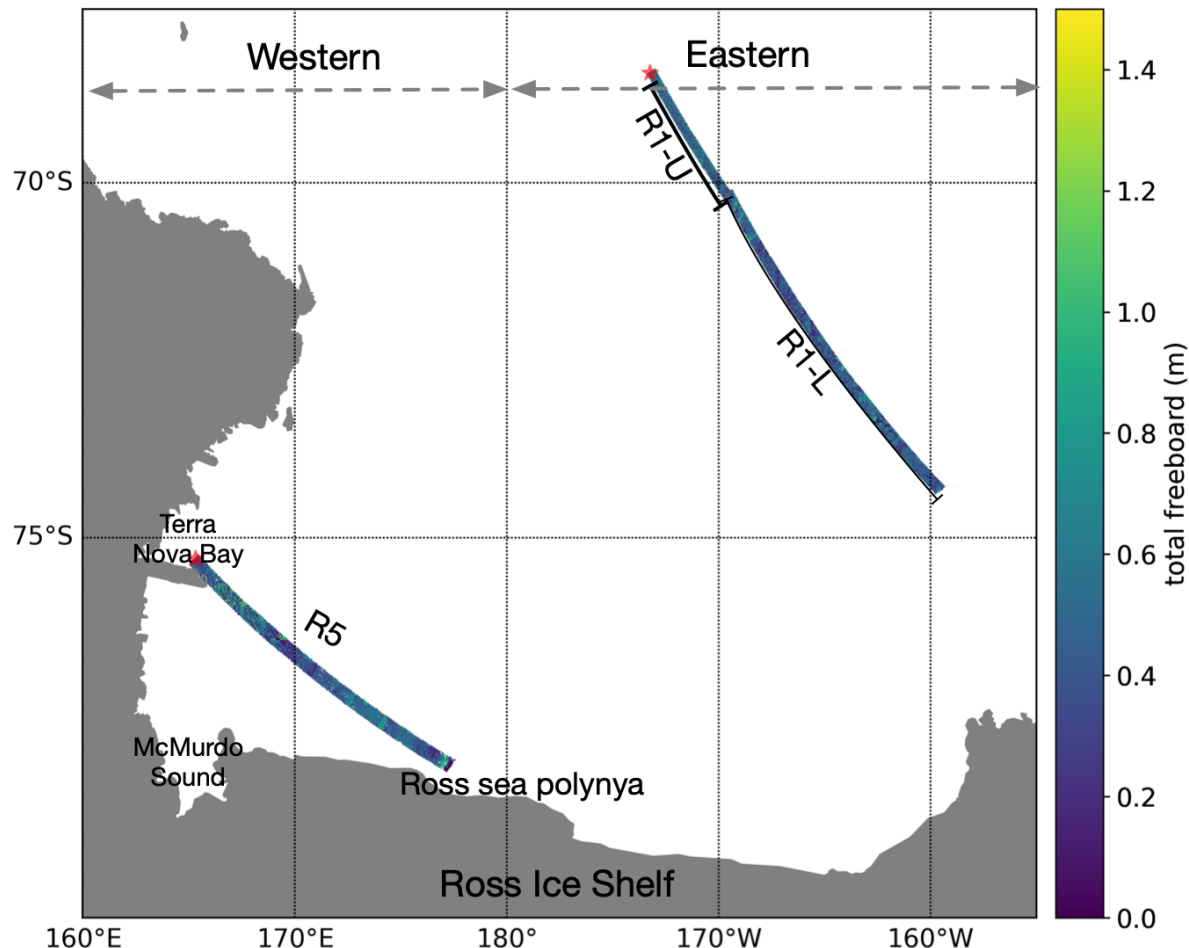


Figure A6. Sea ice DEM ($h_{\text{mod, SAR}}$) over the Ross Sea retrieved from SAR images. The northernmost locations on each segment are marked with star symbols and serve as reference points for calculating the relative distance. $h_{\text{mod, SAR}}$ was downsampled to 500 m pixel size.

565 *Data availability.* TanDEM-X imagery can be acquired from the German Aerospace Center (DLR) by submitting a scientific proposal, accessible at <https://eoweb.dlr.de>. Additionally, DMS data can be obtained from the National Snow and Ice Data Center at <https://nsidc.org/data/icebridge>, while Ice Charts data are available at <https://nsidc.org/data/G10033/versions/1>, also from the National Snow and Ice Data Center.

Author contributions. LH carried out SAR image processing, designed the methodology, analyzed the results, and drafted the manuscript. IH provided valuable input on method development and result analysis, contributing to the enhancement of the manuscript.

570 *Competing interests.* The authors have no conflicts of interest to disclose.

Acknowledgements. The authors would like to thank all individuals involved in the OTASC campaign, jointly conducted by DLR and NASA. Special thanks are extended to Dr. Thomas Busche for his invaluable assistance in accessing the TanDEM-X data.

References

Breiman, L.: Random forests, *Machine learning*, 45, 5–32, <https://doi.org/10.1023/A:1010933404324>, 2001.

575 Castellani, G., Lüpkes, C., Hendricks, S., and Gerdes, R.: Variability of Arctic sea-ice topography and its impact on the atmospheric surface drag, *J. Geophys. Res.: Oceans*, 119, 6743–6762, <https://doi.org/10.1002/2013JC009712>, 2014.

Cloude, S.: Polarisation: applications in remote sensing, Oxford University Press, <https://doi.org/10.1093/acprof:oso/9780199569731.001.0001>, 2010.

Dall, J.: InSAR elevation bias caused by penetration into uniform volumes, *IEEE Trans. Geosci. Remote Sens.*, 45, 2319–2324, <https://doi.org/10.1109/TGRS.2007.896613>, 2007.

580 Dammann, D. O., Eicken, H., Mahoney, A. R., Saito, E., Meyer, F. J., John, C., et al.: Traversing sea ice—linking surface roughness and ice trafficability through SAR polarimetry and interferometry, *IEEE J. Sel. Top. Appl. Earth Obs. Remote Sens.*, 11, 416–433, <https://doi.org/10.1109/JSTARS.2017.2764961>, 2017.

Davis, N. and Wadhams, P.: A statistical analysis of Arctic pressure ridge morphology, *J. Geophys. Res.: Oceans*, 100, 10 915–10 925, <https://doi.org/10.1029/95JC00007>, 1995.

585 Dierking, W.: Laser profiling of the ice surface topography during the Winter Weddell Gyre Study 1992, *J. Geophys. Res.: Oceans*, 100, 4807–4820, <https://doi.org/10.1029/94JC01938>, 1995.

Dierking, W., Lang, O., and Busche, T.: Sea ice local surface topography from single-pass satellite InSAR measurements: a feasibility study, *The Cryosphere*, 11, 1967–1985, <https://doi.org/10.5194/tc-11-1967-2017>, 2017.

590 Dominguez, R.: IceBridge DMS L1B geolocated and orthorectified Images, Version 1, Boulder, Colorado USA: NASA National Snow and Ice Data Center Distributed Active Archive Center, <https://doi.org/10.5067/OZ6VNOPMPRJ0>, accessed Nov 22, 2018., 2010, updated 2018.

Dotson, R. and Arvesen., J.: IceBridge DMS L3 photogrammetric DEM, version 1., Boulder, Colorado USA: NASA National Snow and Ice Data Center Distributed Active Archive Center, <https://doi.org/10.5067/39Y05T544XCC>, accessed Nov 22, 2018., 2012, updated 2014.

595 Duncan, K. and Farrell, S. L.: Determining Variability in Arctic Sea Ice Pressure Ridge Topography With ICESat-2, *Geophys. Res. Lett.*, 49, e2022GL100272, <https://doi.org/10.1029/2022GL100272>, 2022.

Eineder, M., Fritz, T., Mittermayer, J., Roth, A., Boerner, E., and Breit, H.: TerraSAR-X ground segment, basic product specification document, Tech. rep., Cluster Applied Remote Sensing (CAF) Oberpfaffenhofen (Germany), 2008.

Foley, J. P. and Dorsey, J. G.: A review of the exponentially modified Gaussian (EMG) function: evaluation and subsequent calculation of universal data, *J. Chromatogr. Sci.*, 22, 40–46, <https://doi.org/10.1093/chromsci/22.1.40>, 1984.

600 Gaddum, J. H.: Lognormal distributions, *Nature*, 156, 463–466, <https://doi.org/10.1038/156463a0>, 1945.

Garbrecht, T., Lüpkes, C., Hartmann, J., and Wolff, M.: Atmospheric drag coefficients over sea ice—validation of a parameterisation concept, *Tellus A: Dynamic Meteorology and Oceanography*, 54, 205–219, <https://doi.org/10.3402/tellusa.v54i2.12129>, 2002.

Guneriussen, T., Hogda, K. A., Johnsen, H., and Lauknes, I.: InSAR for estimation of changes in snow water equivalent of dry snow, *IEEE Trans Geosci Remote Sens.*, 39, 2101–2108, <https://doi.org/10.1109/36.957273>, 2001.

Haas, C., Quanhua, L., and Thomas, M.: Retrieval of Antarctic sea-ice pressure ridge frequencies from ERS SAR imagery by means of in situ laser profiling and usage of a neural network, *International Journal of Remote Sensing*, 20, 3111–3123, 1999.

605 Hallikainen, M. and Winebrenner, D. P.: The physical basis for sea ice remote sensing, *Microwave remote sensing of sea ice*, 68, 29–46, <https://doi.org/10.1029/GM068p0029>, 1992.

610 Hollands, T. and Dierking, W.: Dynamics of the Terra Nova Bay Polynya: The potential of multi-sensor satellite observations, *Remote Sens. Environ.*, 187, 30–48, <https://doi.org/10.1016/j.rse.2016.10.003>, 2016.

Huang, L. and Hajnsek, I.: Polarimetric Behavior for the Derivation of Sea Ice Topographic Height From TanDEM-X Interferometric SAR Data, *IEEE J. Sel. Top. Appl. Earth Obs. Remote Sens.*, 14, 1095–1110, <https://doi.org/10.1109/JSTARS.2020.3036395>, 2021.

Huang, L., Fischer, G., and Hajnsek, I.: Antarctic snow-covered sea ice topography derivation from TanDEM-X using polarimetric SAR interferometry, *The Cryosphere*, 15, 5323–5344, <https://doi.org/10.5194/tc-15-5323-2021>, 2021.

615 Huang, L., Hajnsek, I., and Nghiem, S. V.: Sea ice elevation in the Western Weddell Sea, Antarctica: Observations from field campaign, *Earth Space Sci.*, 9, e2022EA002472, <https://doi.org/10.1029/2022EA002472>, 2022.

Hughes, B.: On the use of lognormal statistics to simulate one-and two-dimensional under-ice draft profiles, *J. Geophys. Res.: Oceans*, 96, 22 101–22 111, <https://doi.org/10.1029/91JC02336>, 1991.

620 Iacozza, J. and Barber, D. G.: An examination of the distribution of snow on sea-ice, *Atmosphere-Ocean*, 37, 21–51, <https://doi.org/10.1080/07055900.1999.9649620>, 1999.

Kacimi, S. and Kwok, R.: The Antarctic sea ice cover from ICESat-2 and CryoSat-2: freeboard, snow depth, and ice thickness, *The Cryosphere*, 14, 4453–4474, <https://doi.org/10.5194/tc-14-4453-2020>, 2020.

625 Kim, J.-W., Kim, D.-j., and Hwang, B. J.: Characterization of Arctic sea ice thickness using high-resolution spaceborne polarimetric SAR data, *IEEE Trans. Geosci. Remote Sens.*, 50, 13–22, <https://doi.org/10.1109/TGRS.2011.2160070>, 2011.

Krieger, G., Moreira, A., Fiedler, H., Hajnsek, I., Werner, M., Younis, M., and Zink, M.: TanDEM-X: A satellite formation for high-resolution SAR interferometry, *IEEE Trans. Geosci. Remote Sens.*, 45, 3317–3341, <https://doi.org/10.1109/TGRS.2007.900693>, 2007.

Kurtz, N. T. and Markus, T.: Satellite observations of Antarctic sea ice thickness and volume, *J. Geophys. Res.: Oceans*, 117, <https://doi.org/10.1029/2012JC008141>, 2012.

630 Kwok, R. and Kacimi, S.: Three years of sea ice freeboard, snow depth, and ice thickness of the Weddell Sea from Operation IceBridge and CryoSat-2, *The Cryosphere*, 12, 2789–2801, <https://doi.org/10.5194/tc-12-2789-2018>, 2018.

Landy, J. C., Tsamados, M., and Scharien, R. K.: A facet-based numerical model for simulating SAR altimeter echoes from heterogeneous sea ice surfaces, *IEEE Transactions on Geoscience and Remote Sensing*, 57, 4164–4180, <https://doi.org/10.1109/TGRS.2018.2889763>, 2019.

635 Landy, J. C., Petty, A. A., Tsamados, M., and Stroeve, J. C.: Sea ice roughness overlooked as a key source of uncertainty in CryoSat-2 ice freeboard retrievals, *J. Geophys. Res.: Oceans*, 125, e2019JC015820, <https://doi.org/10.1029/90JC02441>, 2020.

Lange, M. and Eicken, H.: The sea ice thickness distribution in the northwestern Weddell Sea, *J. Geophys. Res.: Oceans*, 96, 4821–4837, 1991.

Lee, J.-S. and Pottier, E.: Polarimetric radar imaging: from basics to applications, CRC press, 2009.

640 Leinss, S., Parrella, G., and Hajnsek, I.: Snow height determination by polarimetric phase differences in X-band SAR data, *IEEE J. Sel. Top. Appl. Earth Obs. Remote Sens.*, 7, 3794–3810, <https://doi.org/10.1109/JSTARS.2014.2323199>, 2014.

Leinss, S., Löwe, H., Proksch, M., Lemmetyinen, J., Wiesmann, A., and Hajnsek, I.: Anisotropy of seasonal snow measured by polarimetric phase differences in radar time series, *The Cryosphere*, 10, 1771–1797, <https://doi.org/10.5194/tc-10-1771-2016>, 2016.

López-Dekker, P., Prats, P., De Zan, F., Schulze, D., Krieger, G., and Moreira, A.: TanDEM-X first DEM acquisition: A crossing orbit experiment, *IEEE Geoscience and Remote Sensing Letters*, 8, 943–947, 2011.

645 Madsen, S. N.: Imaging radar interferometry, *Principles and Applications of Imaging Radar*, *Manual of Remote Sensing*, 2, 359–380, 1998.

Massey Jr, F. J.: The Kolmogorov-Smirnov test for goodness of fit, *Journal of the American statistical Association*, 46, 68–78, <https://doi.org/10.1080/01621459.1951.10500769>, 1951.

Massom, R. A., Eicken, H., Hass, C., Jeffries, M. O., Drinkwater, M. R., Sturm, M., Worby, A. P., Wu, X., Lytle, V. I., Ushio, S., et al.: Snow
650 on Antarctic sea ice, *Rev. Geophys.*, 39, 413–445, <https://doi.org/10.1029/2000RG000085>, 2001.

Meier, W. N., Markus, T., and Comiso, J. C.: AMSR-E/AMSR2 Unified L3 Daily 12.5 km Brightness Temperatures, Sea Ice Concentration,
Motion & Snow Depth Polar Grids, Version 1, Boulder, Colorado USA: NASA National Snow and Ice Data Center Distributed Active
Archive Center, <https://doi.org/10.5067/RA1MIJOYPK3P>. Accessed Jan 23, 2021., 2018.

Nghiem, S., Kwok, R., Yueh, S., and Drinkwater, M.: Polarimetric signatures of sea ice: 2. Experimental observations, *J. Geophys. Res.:
655 Oceans*, 100, 13 681–13 698, <https://doi.org/10.1080/08843759508947700>, 1995.

Nghiem, S., Busche, T., Kraus, T., Bachmann, M., Kurtz, N., Sonntag, J., Woods, J., Ackley, S., Xie, H., Maksym, T., et al.: Remote
Sensing of Antarctic Sea Ice with Coordinated Aircraft and Satellite Data Acquisitions, in: *IGARSS 2018*, pp. 8531–8534, IEEE,
<https://doi.org/10.1109/IGARSS.2018.8518550>, 2018.

Nghiem, S. V., Huang, L., and Hajnsek, I.: Theory of radar polarimetric interferometry and its application to the retrieval of sea ice elevation
660 in the Western Weddell Sea, *Antarctic, Earth Space Sci.*, 9, e2021EA002 191, <https://doi.org/10.1029/2021EA002191>, 2022.

Petty, A. A., Tsamados, M. C., Kurtz, N. T., Farrell, S. L., Newman, T., Harbeck, J. P., Feltham, D. L., and Richter-Menge, J. A.: Charac-
terizing Arctic sea ice topography using high-resolution IceBridge data, *The Cryosphere*, 10, 1161–1179, [https://doi.org/10.5194/tc-10-1161-2016](https://doi.org/10.5194/tc-10-
1161-2016), 2016.

Rack, W., Price, D., Haas, C., Langhorne, P. J., and Leonard, G. H.: Sea ice thickness in the Western Ross Sea, *Geophys. Res. Lett.*, 48,
665 e2020GL090 866, <https://doi.org/10.1029/2020GL090866>, 2021.

Ressel, R., Singha, S., Lehner, S., Rösel, A., and Spreen, G.: Investigation into different polarimetric features for sea ice
classification using X-band synthetic aperture radar, *IEEE J. Sel. Top. Appl. Earth Obs. Remote Sens.*, 9, 3131–3143,
<https://doi.org/10.1109/JSTARS.2016.2539501>, 2016.

Rosen, P. A., Hensley, S., Joughin, I. R., Li, F. K., Madsen, S. N., Rodriguez, E., and Goldstein, R. M.: Synthetic aperture radar interferometry,
670 *Proceedings of the IEEE*, 88, 333–382, <https://doi.org/10.1109/5.838084>, 2000.

Scott, M.: Understanding climate: Antarctic sea ice extent., NOAA Climate Government, [https://www.climate.gov/news-features/
understanding-climate/understanding-climate-antarctic-sea-ice-extent](https://www.climate.gov/news-features/
understanding-climate/understanding-climate-antarctic-sea-ice-extent), accessed March 22, 2024., 2023.

Sharma, J. J., Hajnsek, I., Papathanassiou, K. P., and Moreira, A.: Estimation of glacier ice extinction using long-wavelength airborne Pol-
InSAR, *IEEE Trans. Geosci. Remote Sens.*, 51, 3715–3732, <https://doi.org/10.1109/TGRS.2012.2220855>, 2012.

Singha, S., Johansson, M., Hughes, N., Hvidgaard, S. M., and Skourup, H.: Arctic Sea Ice Characterization Using Spaceborne Fully Po-
675 larimetric L-, C-, and X-band SAR With Validation by Airborne Measurements, *IEEE Trans. Geosci. Remote Sens.*, 56, 3715–3734,
<https://doi.org/10.1109/TGRS.2018.2809504>, 2018.

Tian, L., Xie, H., Ackley, S. F., Tang, J., Mestas-Nuñez, A. M., and Wang, X.: Sea-ice freeboard and thickness in the Ross Sea from airborne
(IceBridge 2013) and satellite (ICESat 2003–2008) observations, *Ann. Glaciol.*, 61, 24–39, <https://doi.org/10.1017/aog.2019.49>, 2020.

Tin, T. and Jeffries, M. O.: Sea-ice thickness and roughness in the Ross Sea, Antarctica, *Ann. Glaciol.*, 33, 187–193,
680 <https://doi.org/10.3189/172756401781818770>, 2001.

Tison, J.-L., Worby, A., Delille, B., Brabant, F., Papadimitriou, S., Thomas, D., De Jong, J., Lannuzel, D., and Haas, C.: Temporal evolution of
decaying summer first-year sea ice in the Western Weddell Sea, Antarctica, *Deep Sea Research Part II: Topical Studies in Oceanography*,
55, 975–987, 2008.

685 Trujillo, E., Leonard, K., Maksym, T., and Lehning, M.: Changes in snow distribution and surface topography following a snowstorm on Antarctic sea ice, *Journal of Geophysical Research: Earth Surface*, 121, 2172–2191, <https://doi.org/10.1002/2016JF003893>, 2016.

U.S. National Ice Center.: U.S. National Ice Center Arctic and Antarctic Sea Ice Charts in SIGRID-3 Format, Version 1, <https://doi.org/10.7265/4b7s-rn93>, 2022.

690 Vernet, M., Geibert, W., Hoppema, M., Brown, P. J., Haas, C., Hellmer, H., Jokat, W., Jullion, L., Mazloff, M., Bakker, D., et al.: The Weddell Gyre, Southern Ocean: present knowledge and future challenges, *Rev. Geophys.*, 57, 623–708, <https://doi.org/10.1029/2018RG000604>, 2019.

Wakabayashi, H., Matsuoka, T., Nakamura, K., and Nishio, F.: Polarimetric Characteristics of sea ice in the sea of Okhotsk observed by airborne L-band SAR, *IEEE Trans. Geosci. Remote Sens.*, 42, 2412–2425, <https://doi.org/10.1109/TGRS.2004.836259>, 2004.

695 Wang, X., Jiang, W., Xie, H., Ackley, S., and Li, H.: Decadal variations of sea ice thickness in the Amundsen-Bellingshausen and Weddell seas retrieved from ICESat and IceBridge laser altimetry, 2003–2017, *J. Geophys. Res.: Oceans*, 125, e2020JC016077, <https://doi.org/10.1029/2020JC016077>, 2020.

Weeks, W. F. and Ackley, S. F.: The growth, structure, and properties of sea ice, in: *The geophysics of sea ice*, pp. 9–164, Springer, https://doi.org/10.1007/978-1-4899-5352-0_2, 1986.

700 Winebrenner, D., Farmer, L., and Joughin, I.: On the response of polarimetric synthetic aperture radar signatures at 24-cm wavelength to sea ice thickness in Arctic leads, *Radio Sci.*, 30, 373–402, <https://doi.org/10.1029/94RS02313>, 1995.

Yi, D., Egido, A., Smith, W. H., Connor, L., Buchhaupt, C., and Zhang, D.: Arctic Sea-Ice Surface Elevation Distribution from NASA's Operation IceBridge ATM Data, *Remote Sensing*, 14, 3011, <https://doi.org/10.3390/rs14133011>, 2022.

705 Yitayew, T. G., Dierking, W., Divine, D. V., Eltoft, T., Ferro-Famil, L., Rösel, A., and Negrel, J.: Validation of Sea-Ice Topographic Heights Derived From TanDEM-X Interferometric SAR Data With Results From Laser Profiler and Photogrammetry, *IEEE Trans. Geosci. Remote Sens.*, 56, 6504–6520, <https://doi.org/10.1109/TGRS.2018.2839590>, 2018.

Zwally, H. J., Yi, D., Kwok, R., and Zhao, Y.: ICESat measurements of sea ice freeboard and estimates of sea ice thickness in the Weddell Sea, *J. Geophys. Res.: Oceans*, 113, <https://doi.org/10.1029/2007JC004284>, 2008.